Supporting Information

Lanthanide Contraction Effects on Structures, Thermostabilities, and CO_2 Adsorption and Separation Behaviors of Isostructural Lanthanide-Organic Frameworks

Weijun Mu,[1] Xin Huang,[2] Ruiqin Zhong,[2] Wei Xia,[1] Jia Liu,[1] Ruqiang Zou[1,]*

[1] *Department of Materials Science and Engineering, College of Engineering, Peking University, Beijing 100871, China. Email: rzou@pku.edu.cn.*

[2] *State Key Laboratory of Heavy Oil Processing, China University of Petroleum, Beijing, 102249, China.*

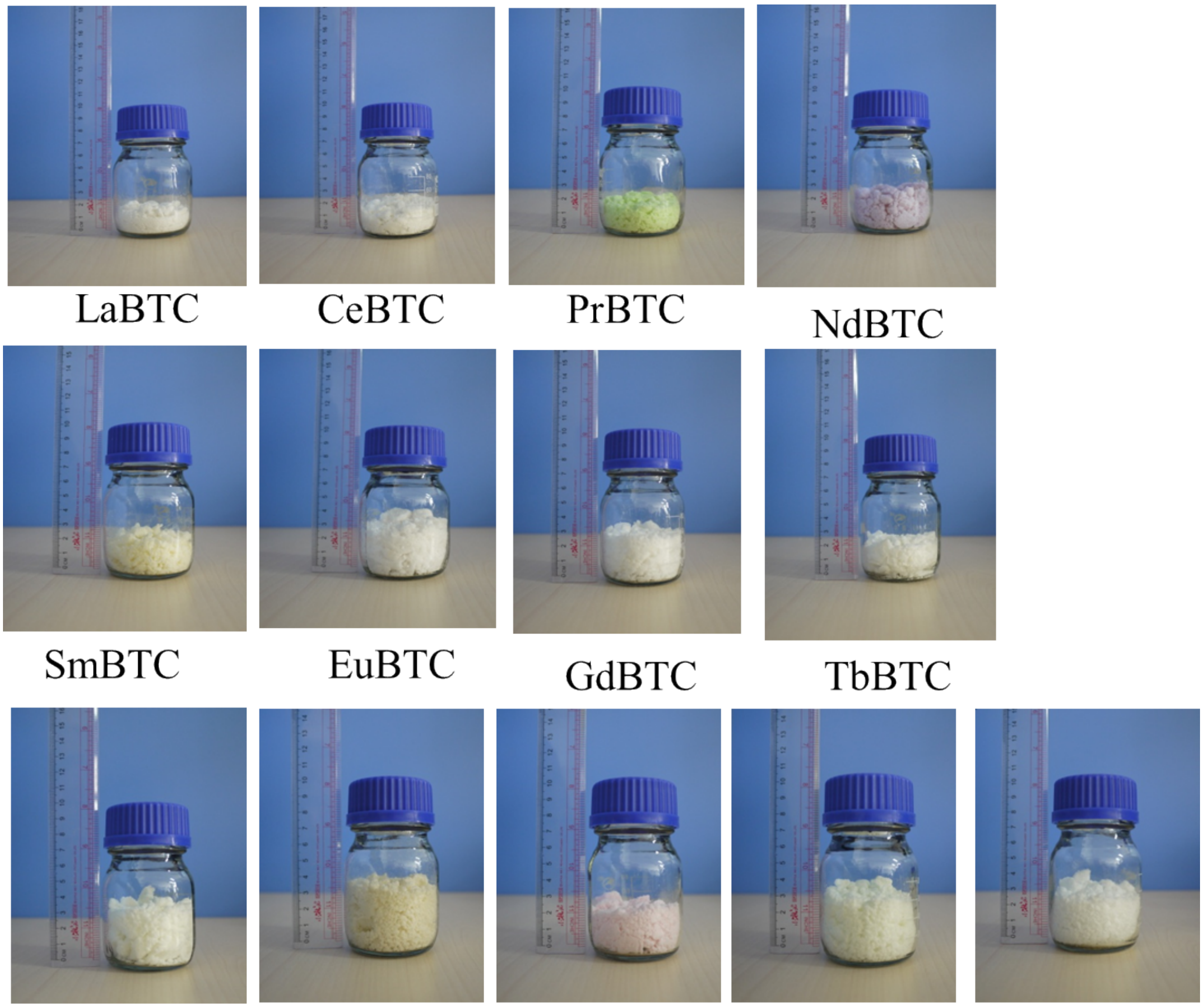

LaBTC CeBTC PrBTC NdBTC

SmBTC EuBTC GdBTC TbBTC

DyBTC HoBTC ErBTC TmBTC YbBTC

Fig. S1. The photographs of synthesized LnBTC.

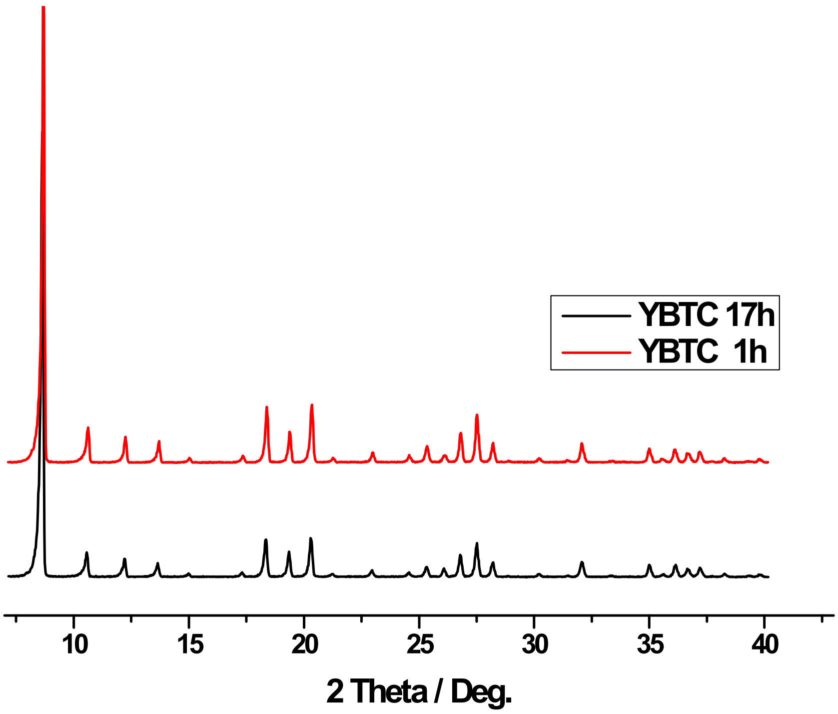

Fig. S2 PXRD patterns of YBTC after the reaction of 1h and 17h, respectively.

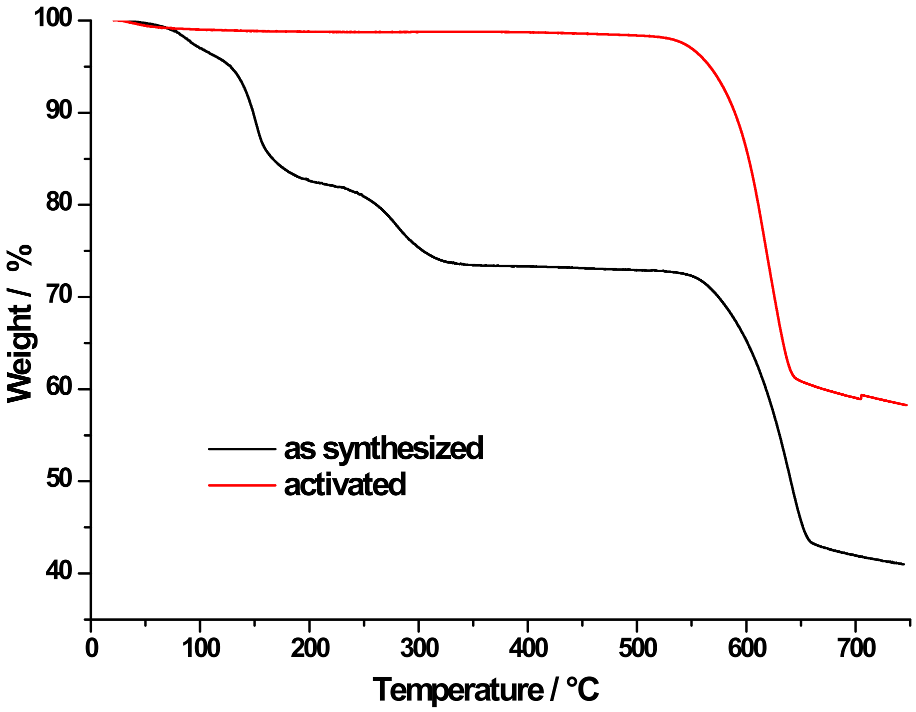

Fig. S3 TG curves of YBTC in flowing nitrogen atmosphere: as synthesized sample (black line) and activated sample treated at 340°C in a vacuum for 6 h (red line).

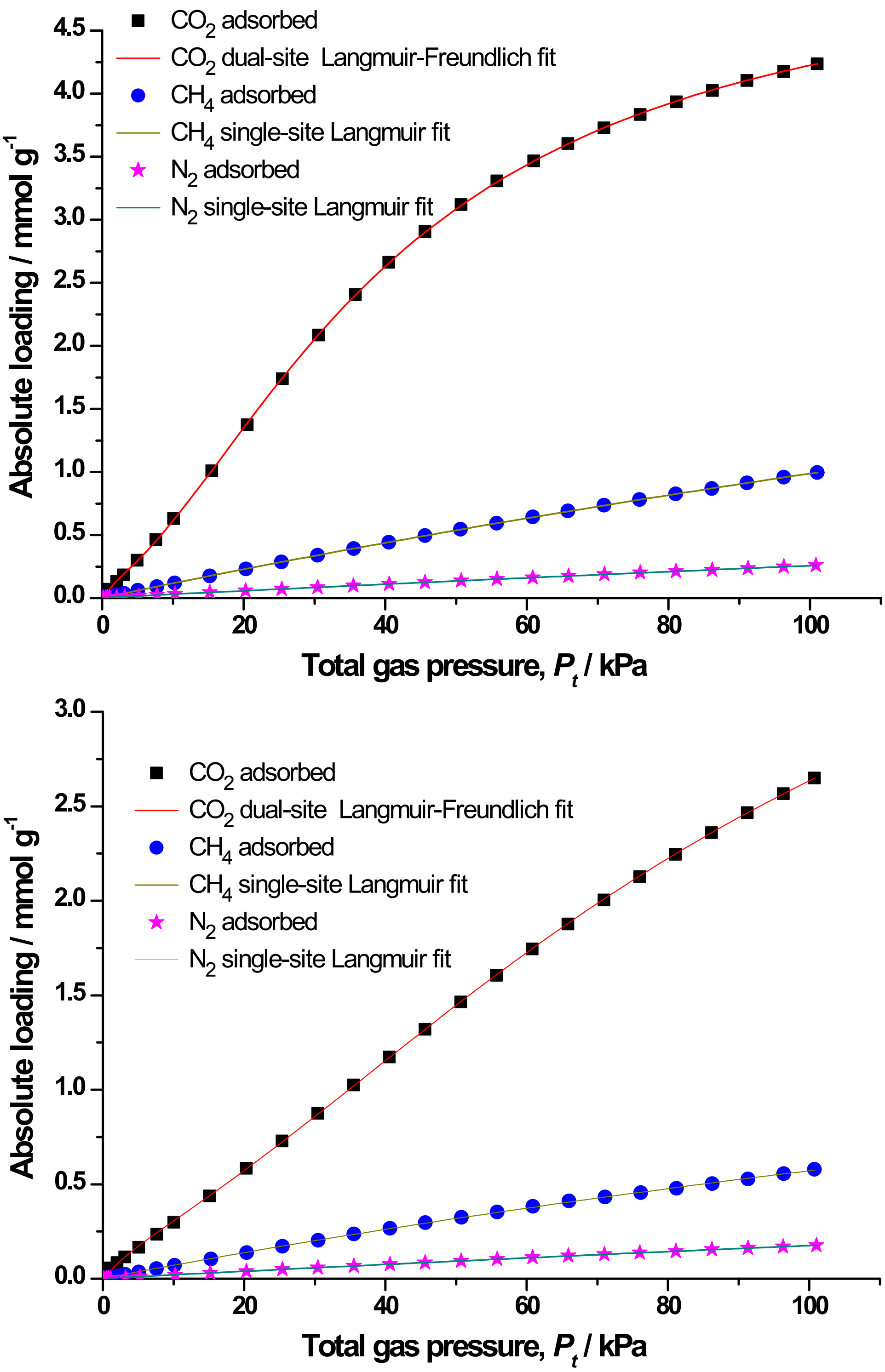

Fig. S4 The pure component isotherm data for carbon dioxide, methane and nitrogen in LaBTC at 273 K (upper) and 298K (lower).

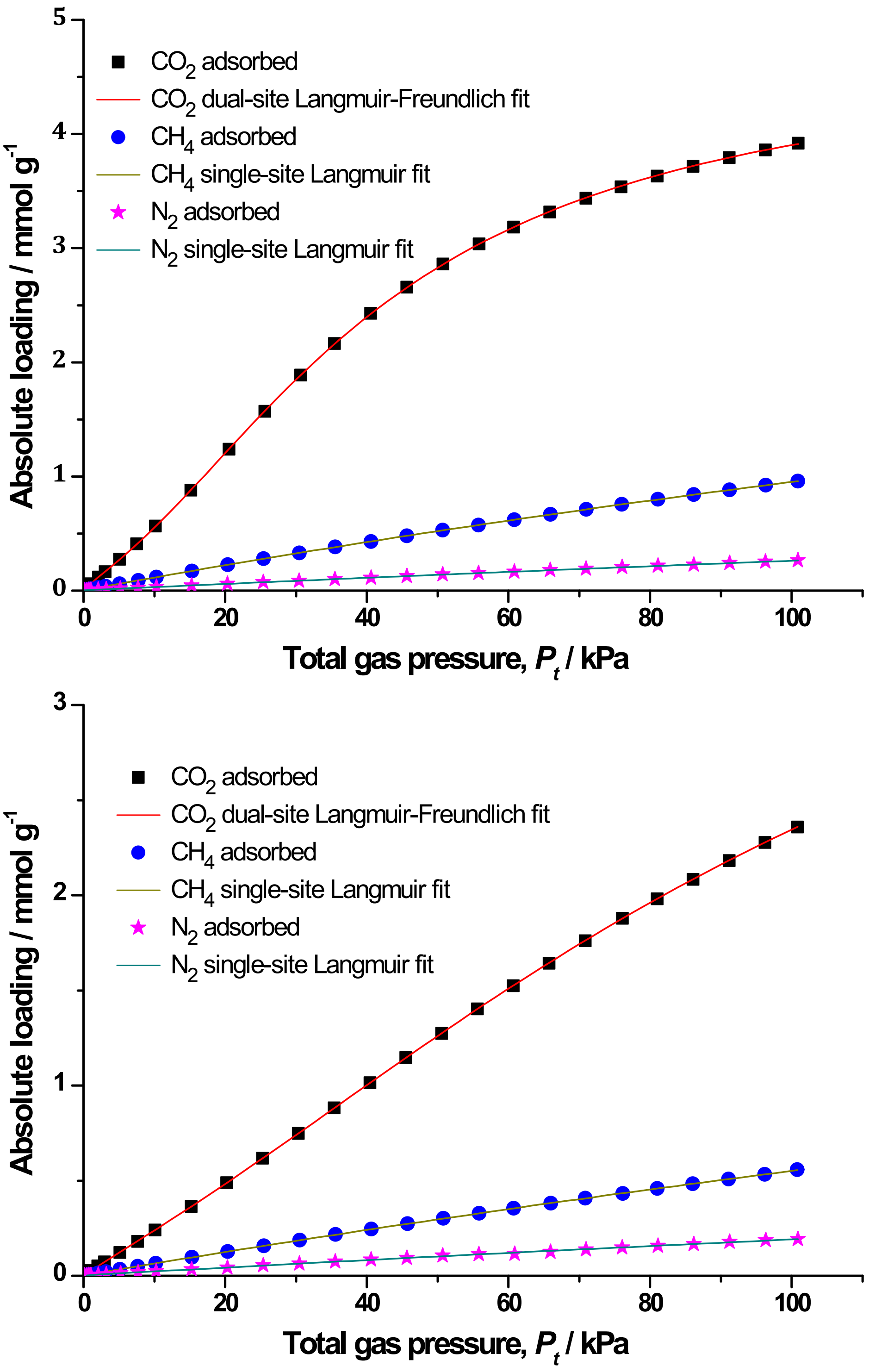

Fig. S5 The pure component isotherm data for carbon dioxide, methane and nitrogen in CeBTC at 273 K (upper) and 298K (lower).

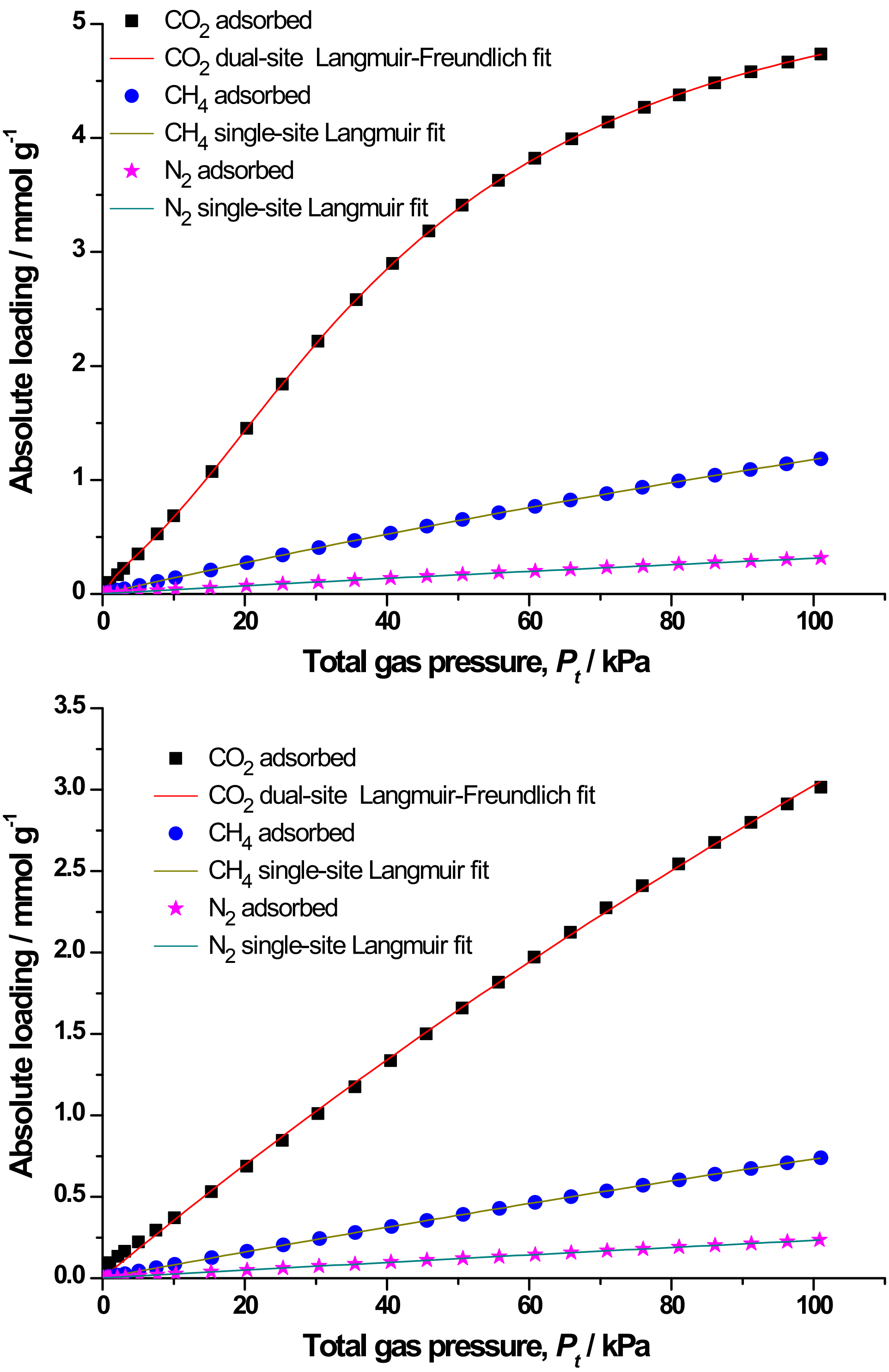

Fig. S6 The pure component isotherm data for carbon dioxide, methane and nitrogen in PrBTC at 273 K (upper) and 298K (lower).

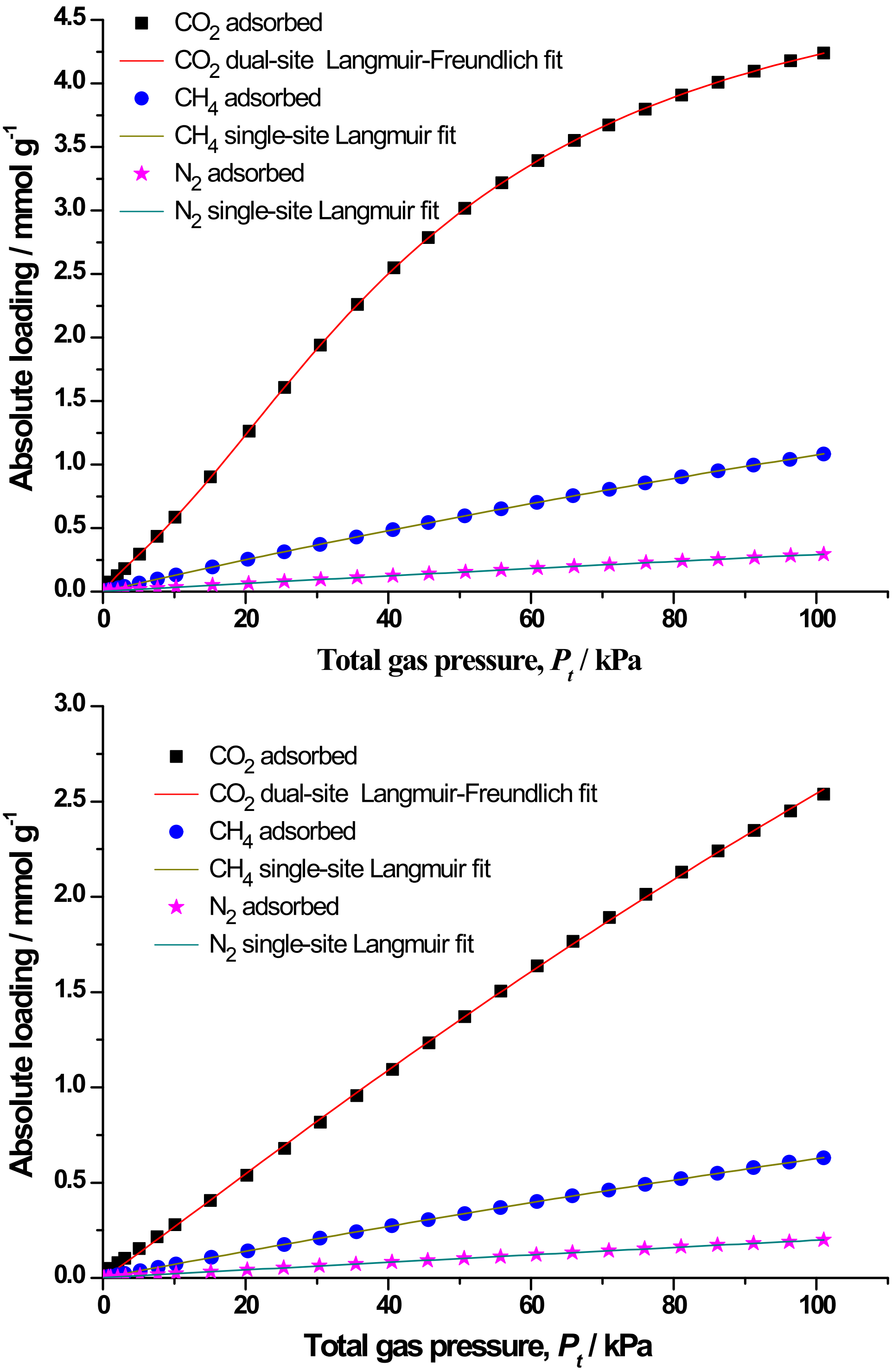

Fig. S7 The pure component isotherm data for carbon dioxide, methane and nitrogen in NdBTC at 273 K (upper) and 298K (lower).

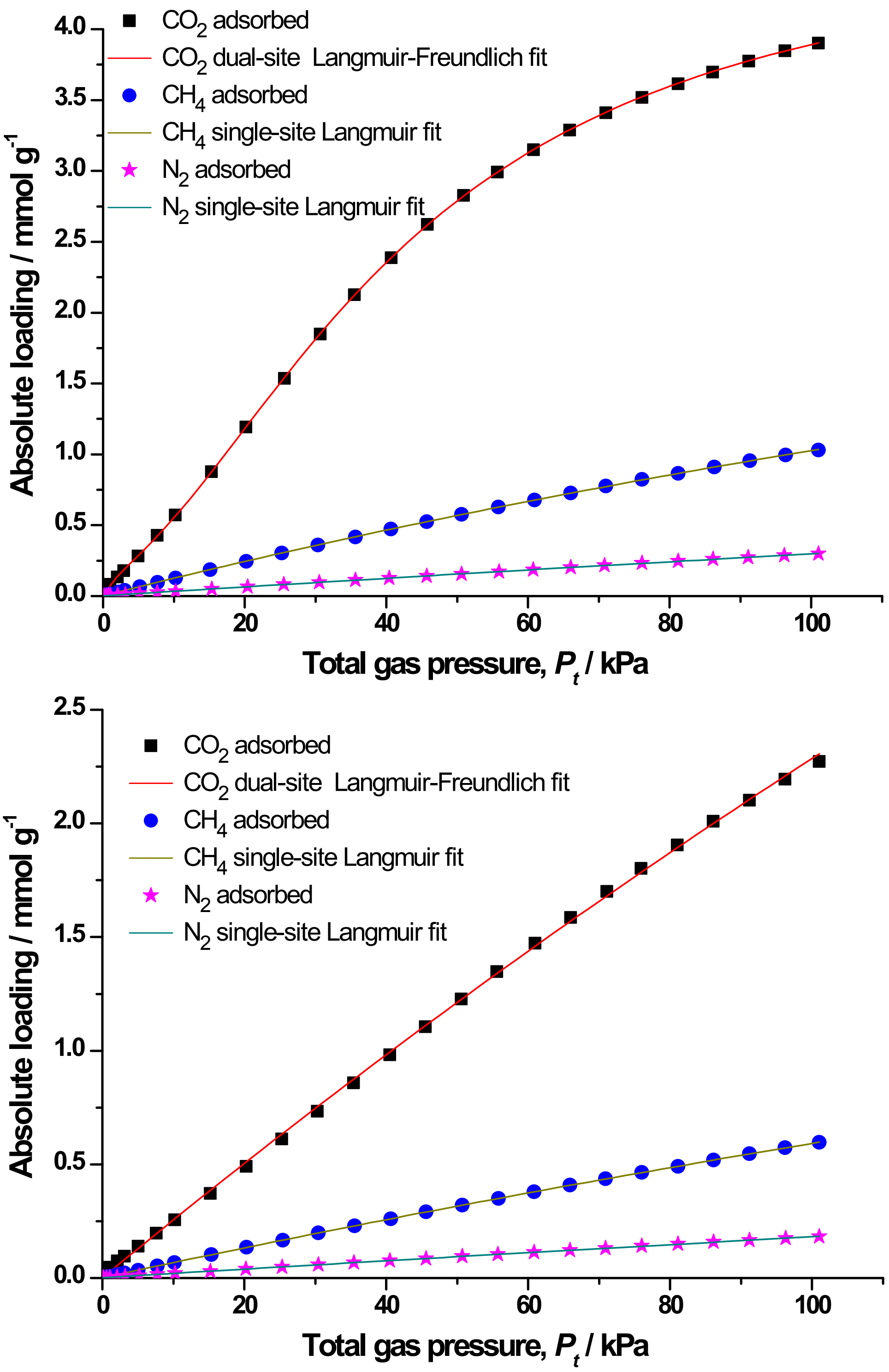

Fig. S8 The pure component isotherm data for carbon dioxide, methane and nitrogen in SmBTC at 273 K (upper) and 298K(lower).

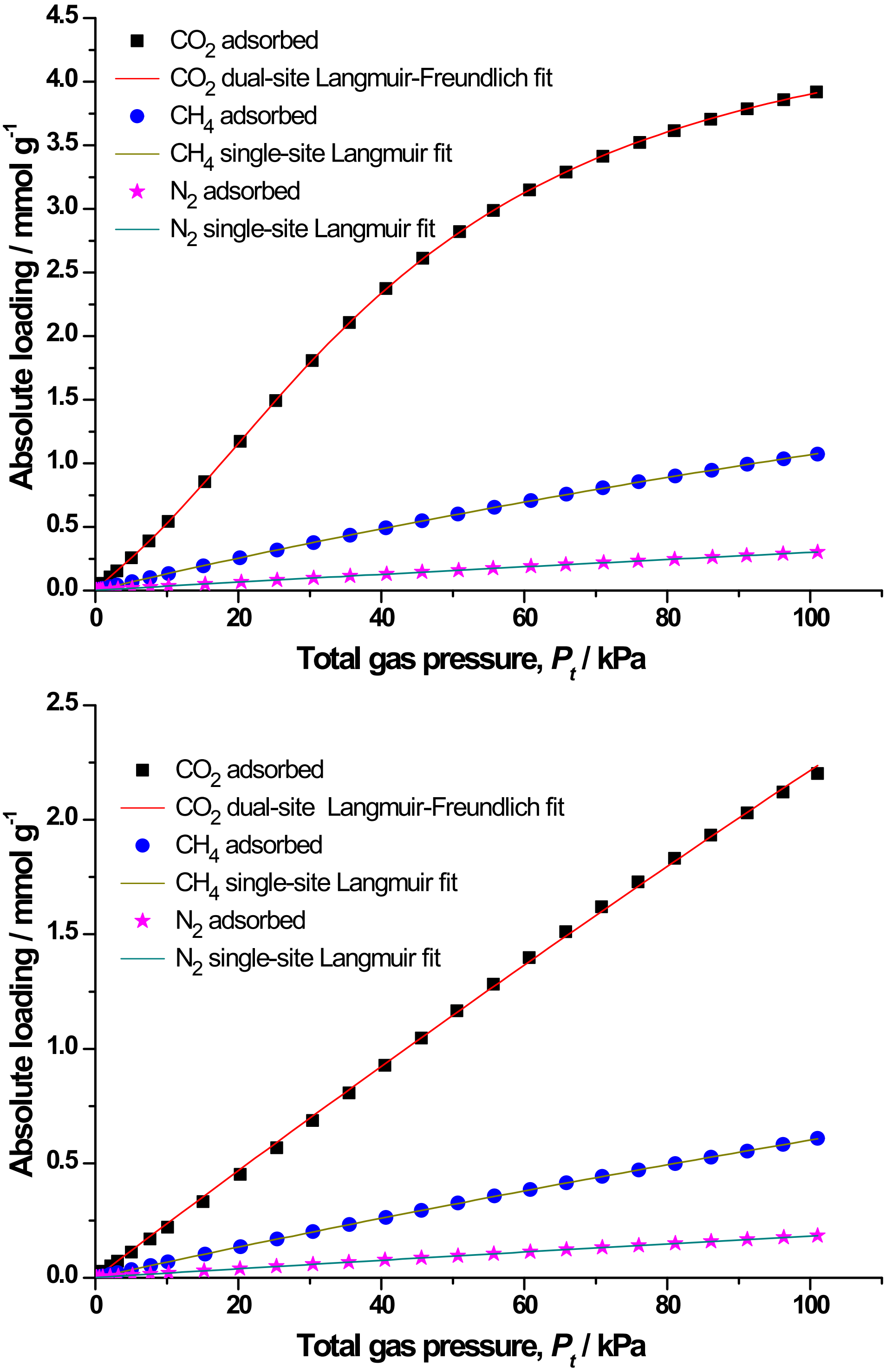

Fig. S9 The pure component isotherm data for carbon dioxide, methane and nitrogen in EuBTC at 273 K (upper) and 298K(lower).

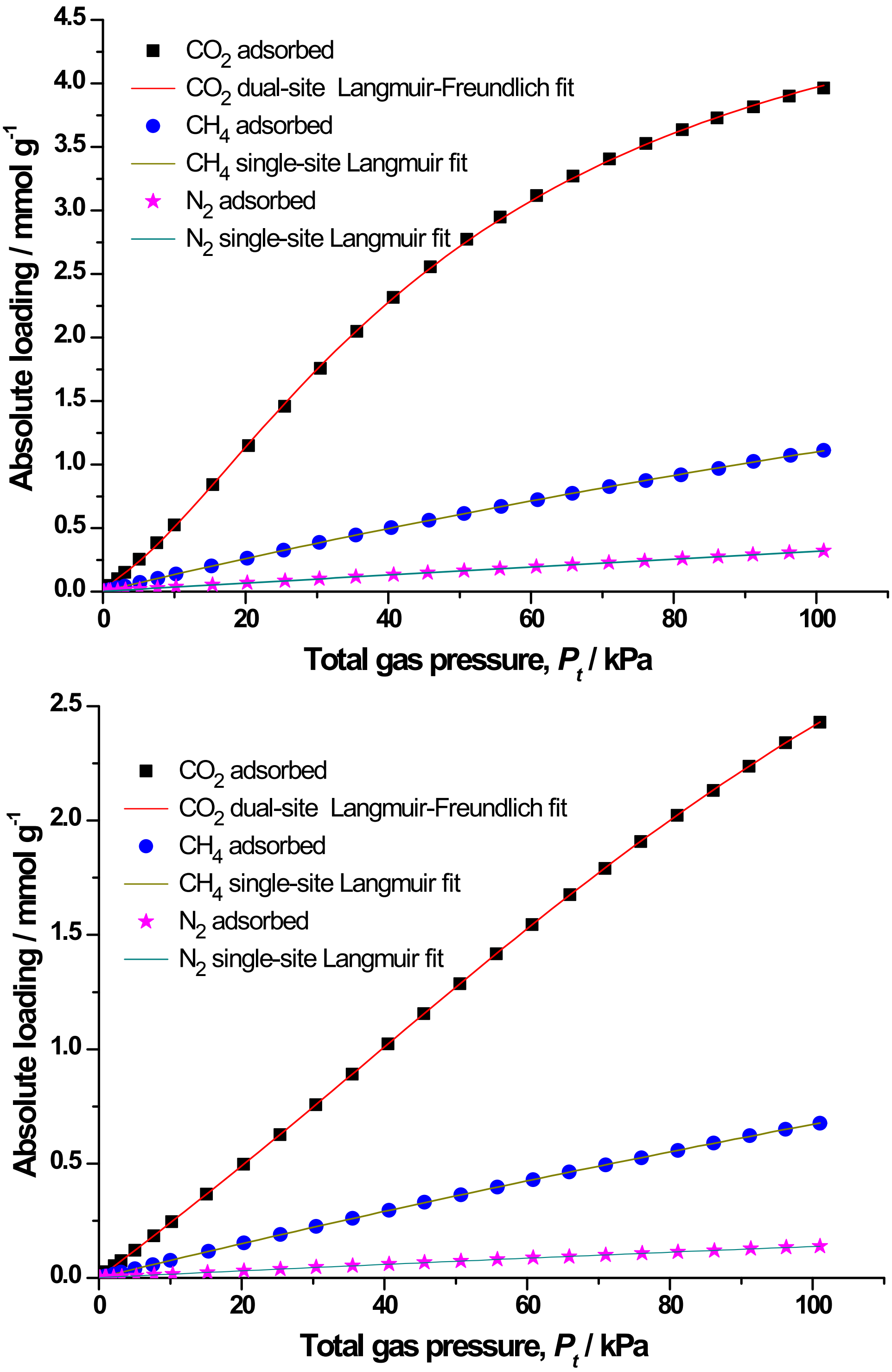

Fig. S10 The pure component isotherm data for carbon dioxide, methane and nitrogen in GdBTC at 273 K (upper) and 298K(lower).

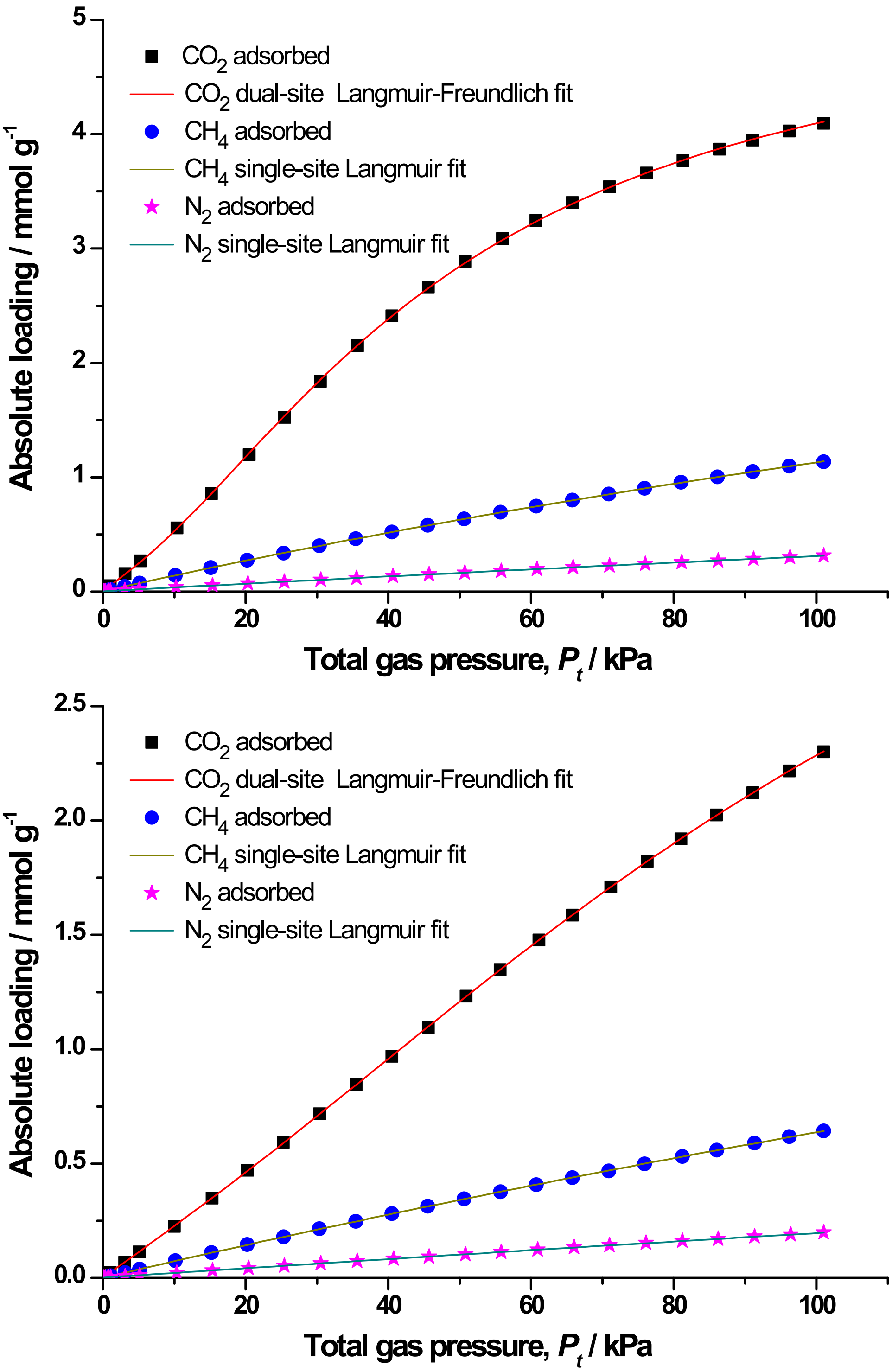

Fig. S11 The pure component isotherm data for carbon dioxide, methane and nitrogen in TbBTC at 273 K (upper) and 298K(lower).

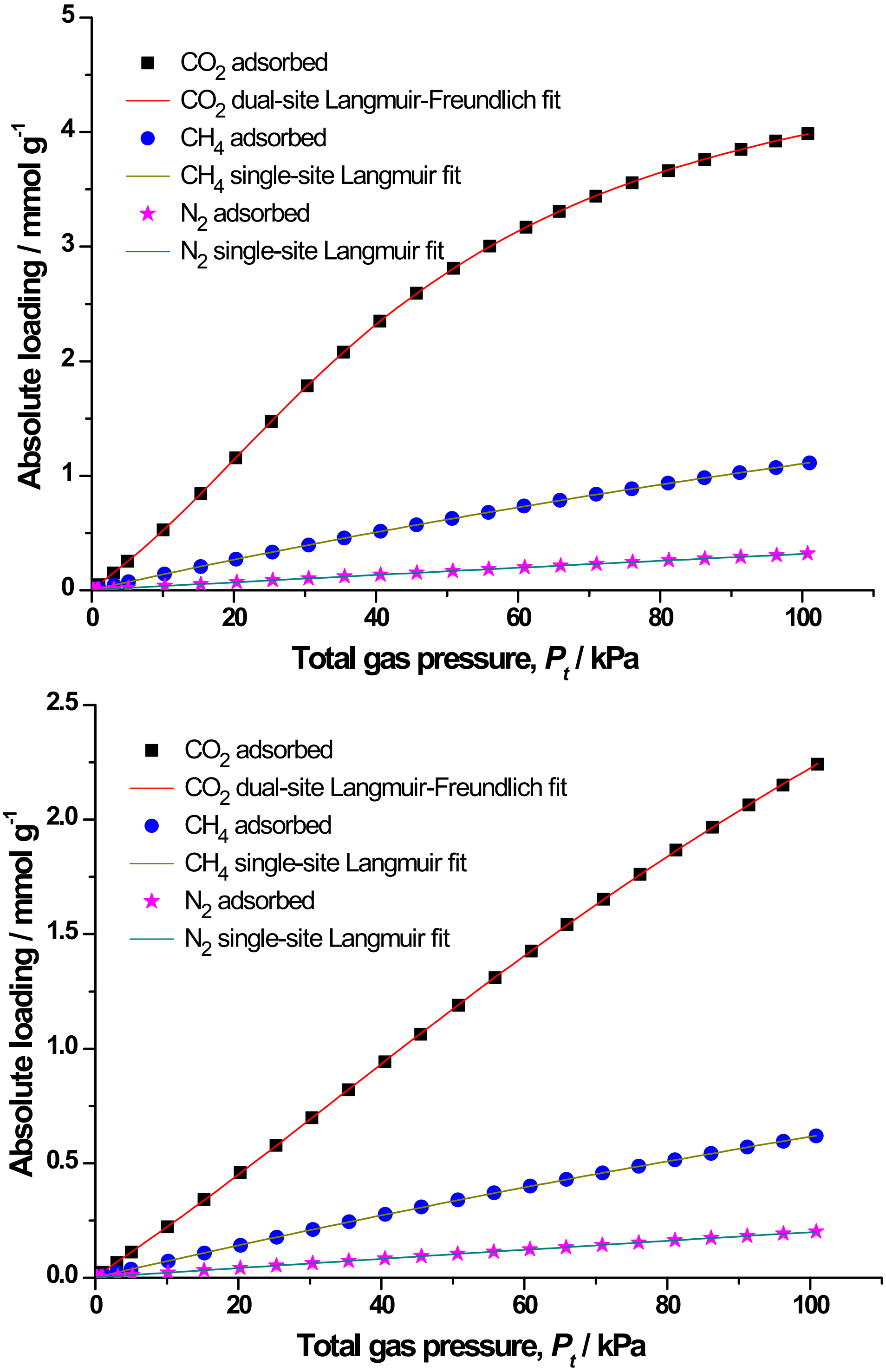

Fig. S12 The pure component isotherm data for carbon dioxide, methane and nitrogen in DyBTC at 273 K (upper) and 298K(lower).

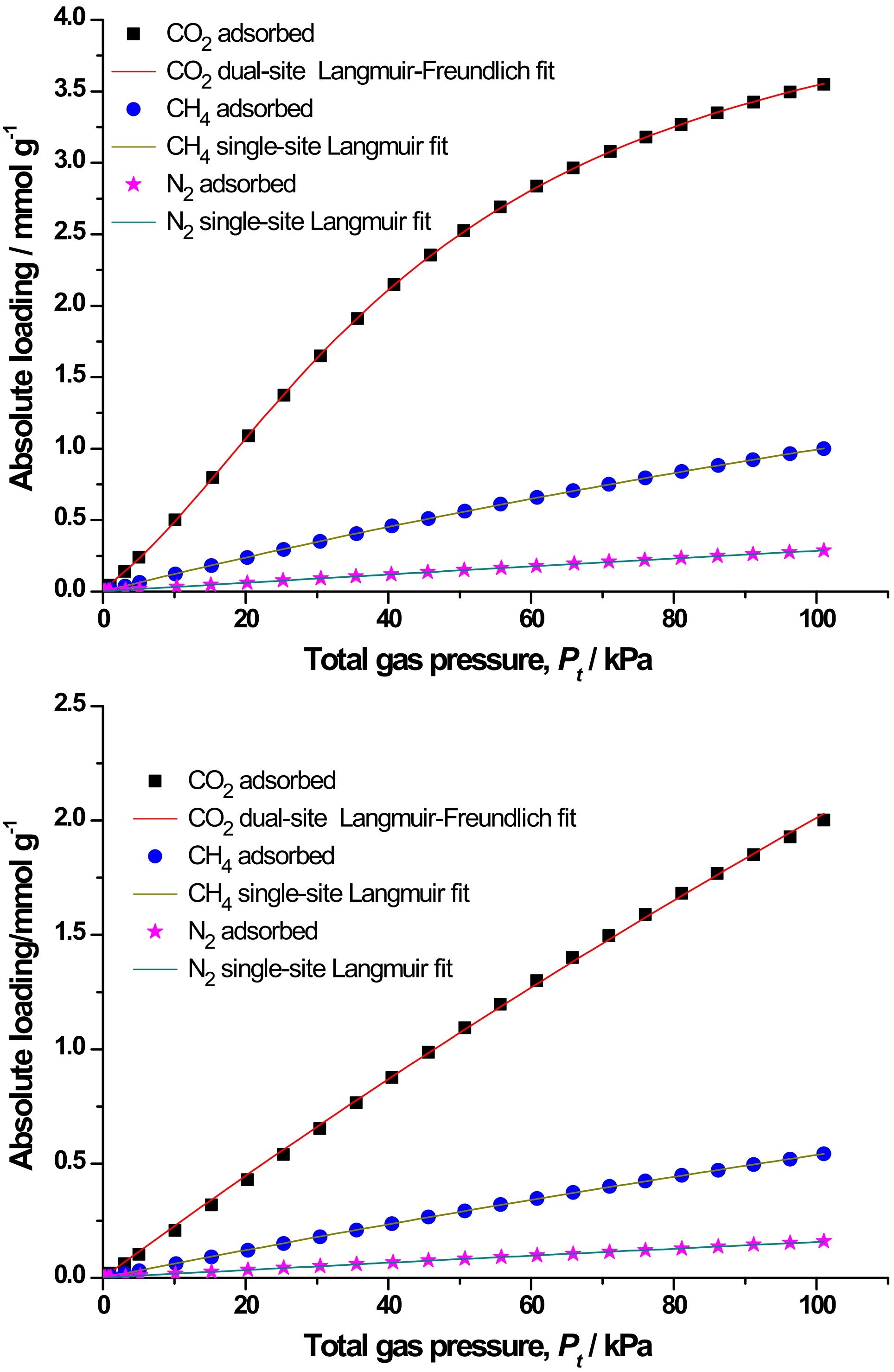

Fig. S13 The pure component isotherm data for carbon dioxide, methane and nitrogen in HoBTC at 273 K (upper) and 298K(lower).

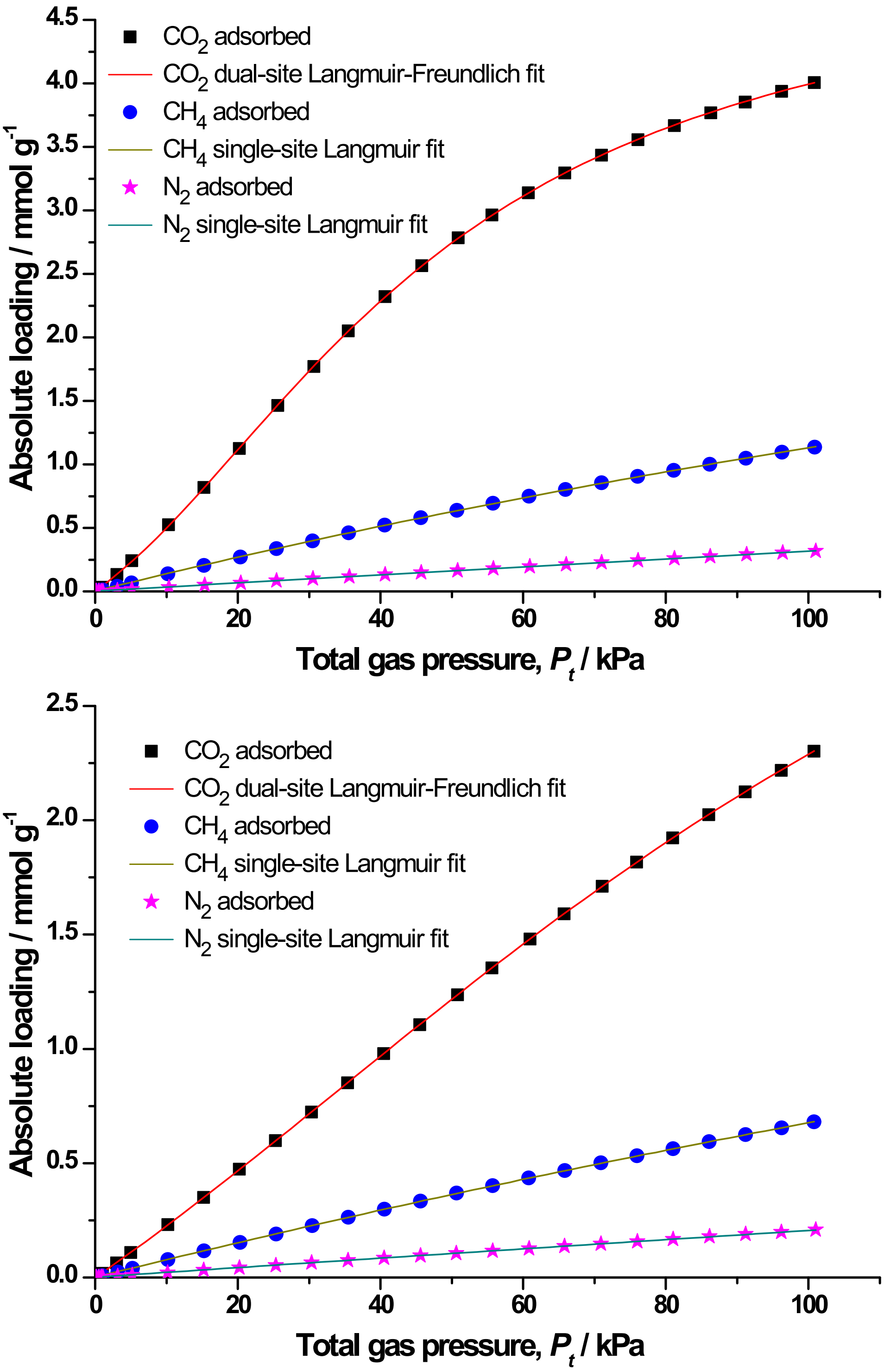

Fig. S14 The pure component isotherm data for carbon dioxide, methane and nitrogen in ErBTC at 273 K (upper) and 298K(lower).

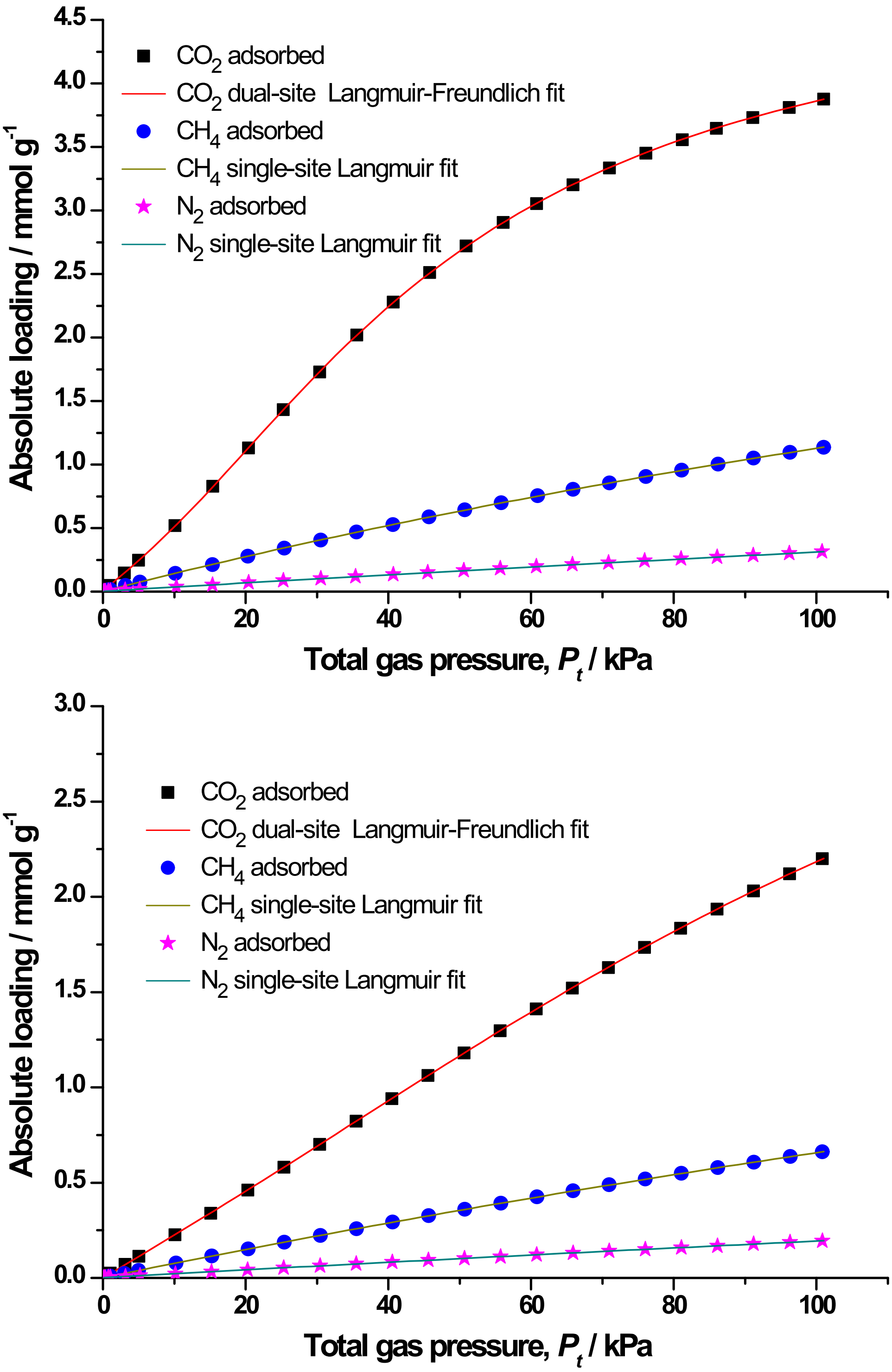

Fig. S15 The pure component isotherm data for carbon dioxide, methane and nitrogen in TmBTC at 273 K (upper) and 298K(lower).

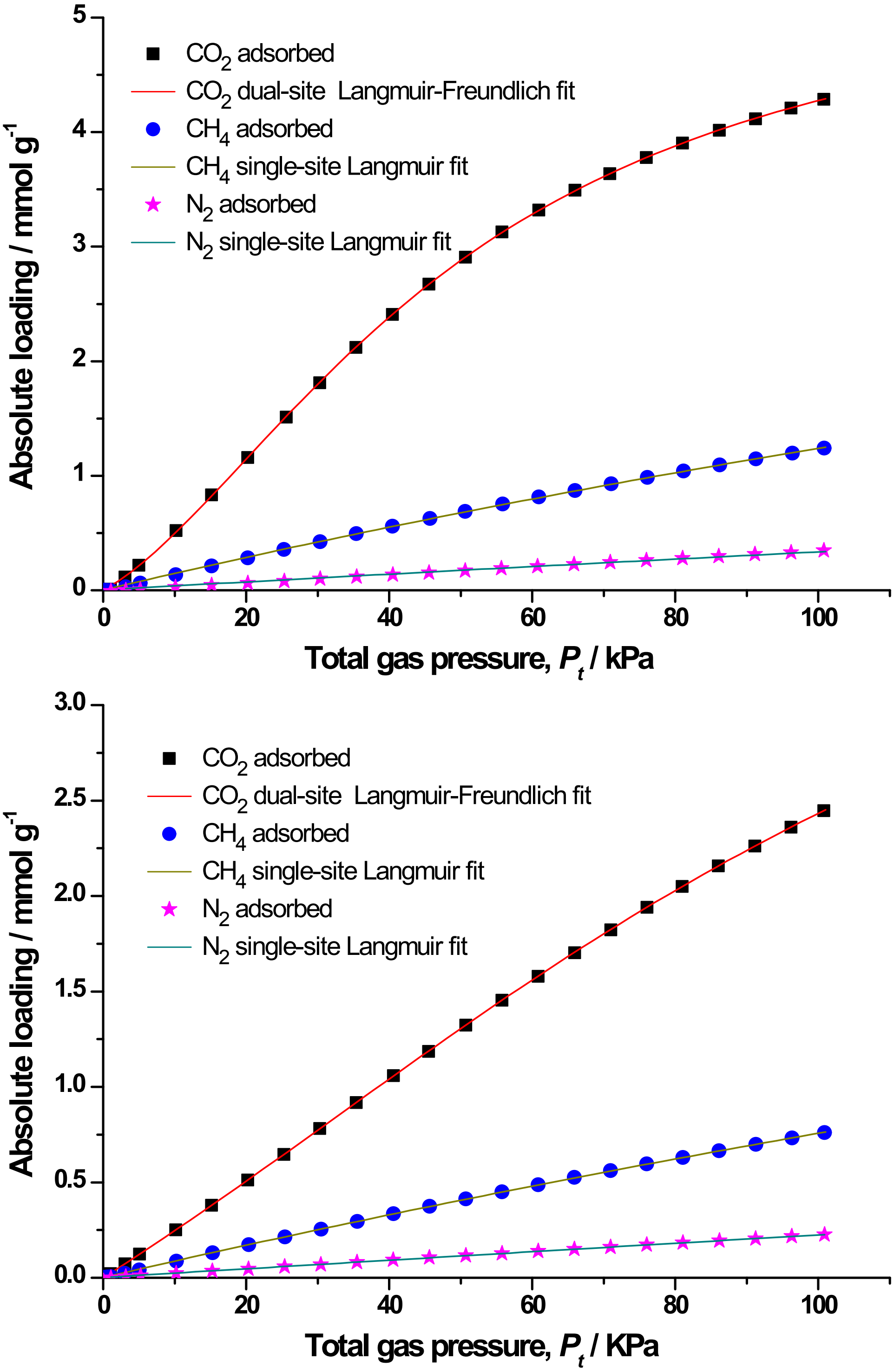

Fig. S16 The pure component isotherm data for carbon dioxide, methane and nitrogen in YbBTC at 273 K (upper) and 298K(lower).

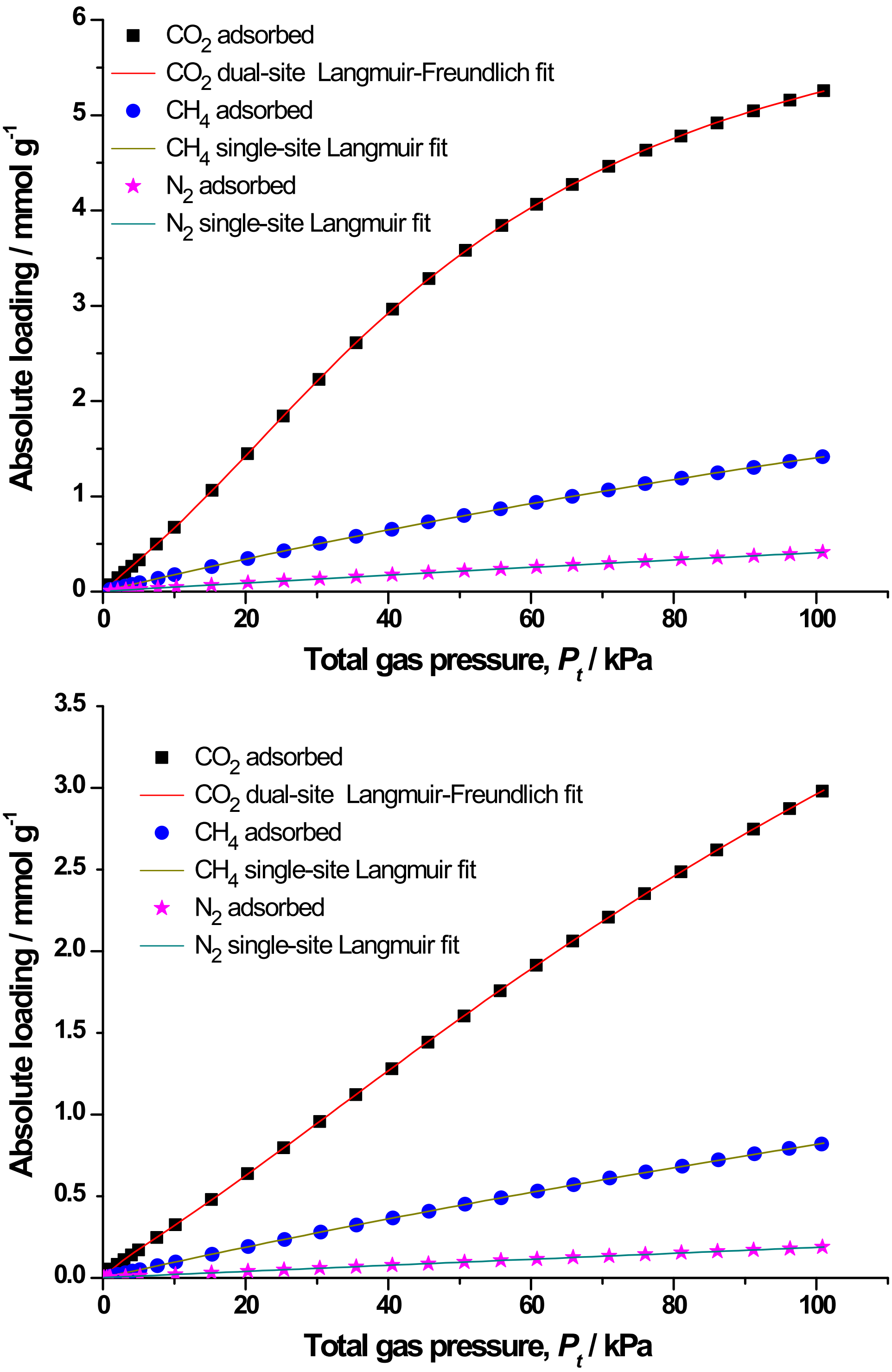

Fig. S17 The pure component isotherm data for carbon dioxide, methane and nitrogen in YBTC at 273 K (upper) and 298K(lower).

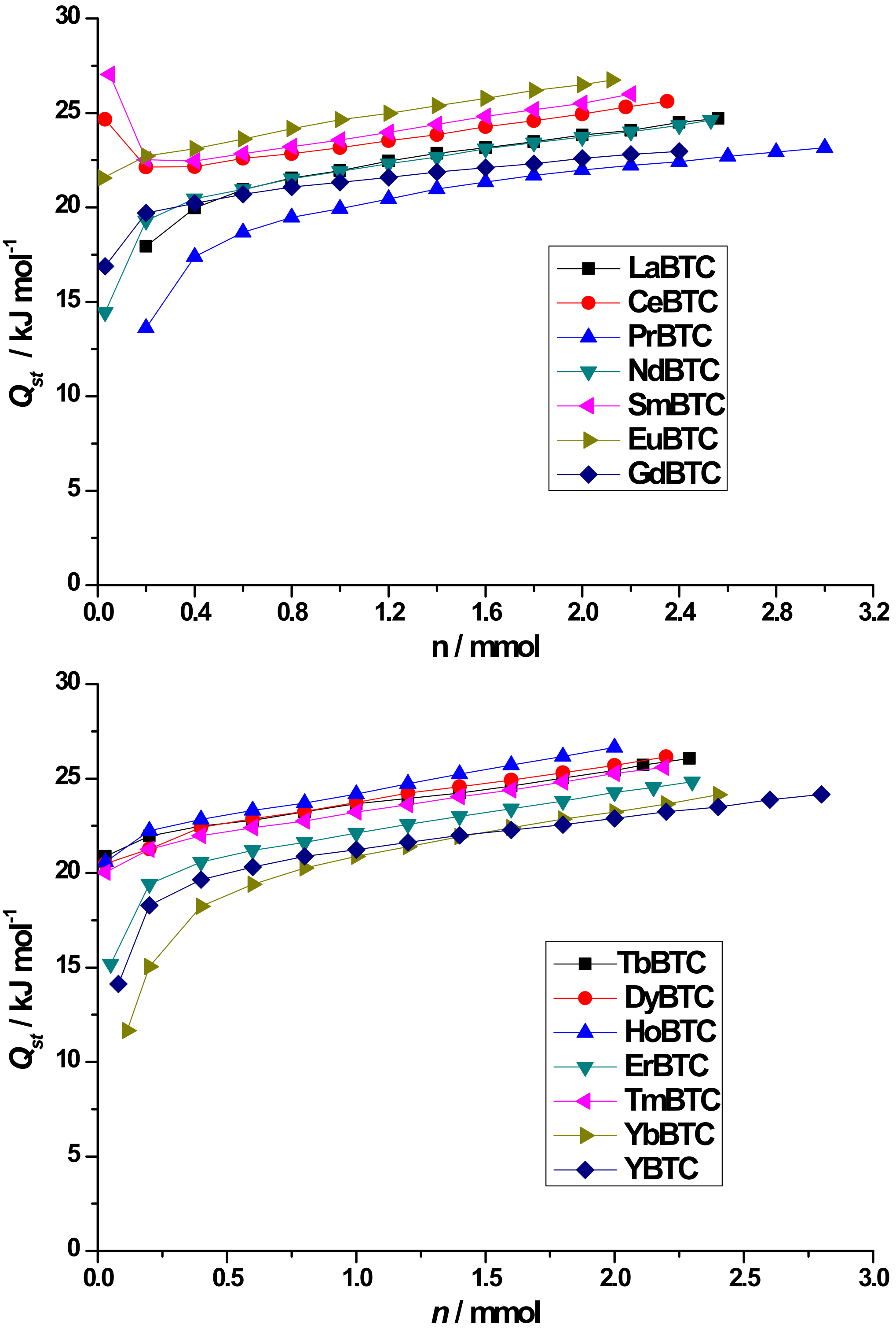

Fig. S18 Isosteric heats of CO_2 absorption of LnBTCs.

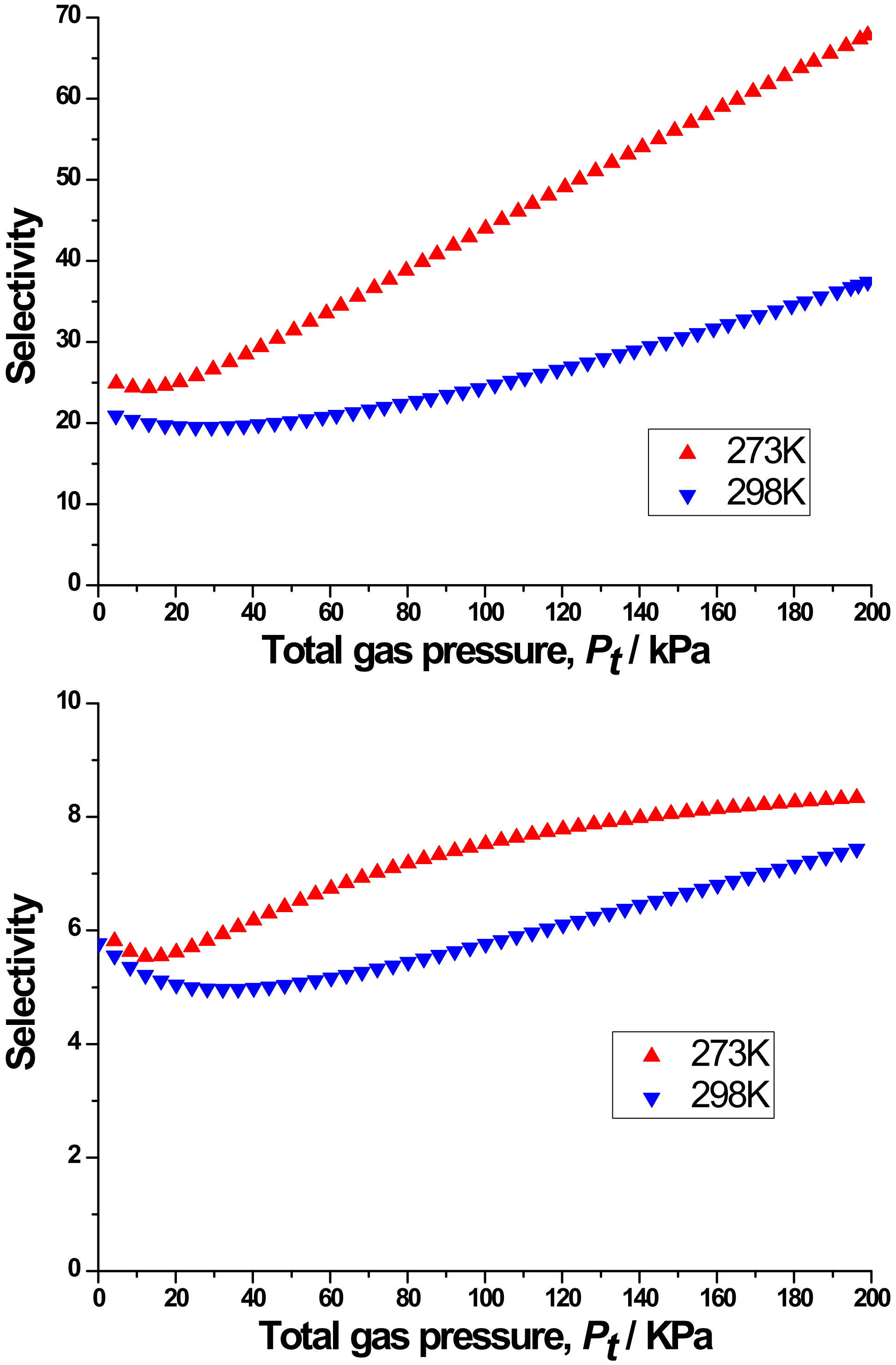

Fig. S19 Calculations of the adsorption selectivity, S_{ads}, using Ideal Adsorbed Solution Theory(IAST) for carbon dioxide/nitrogen (upper) and carbon dioxide/methane (lower) in LaBTC.

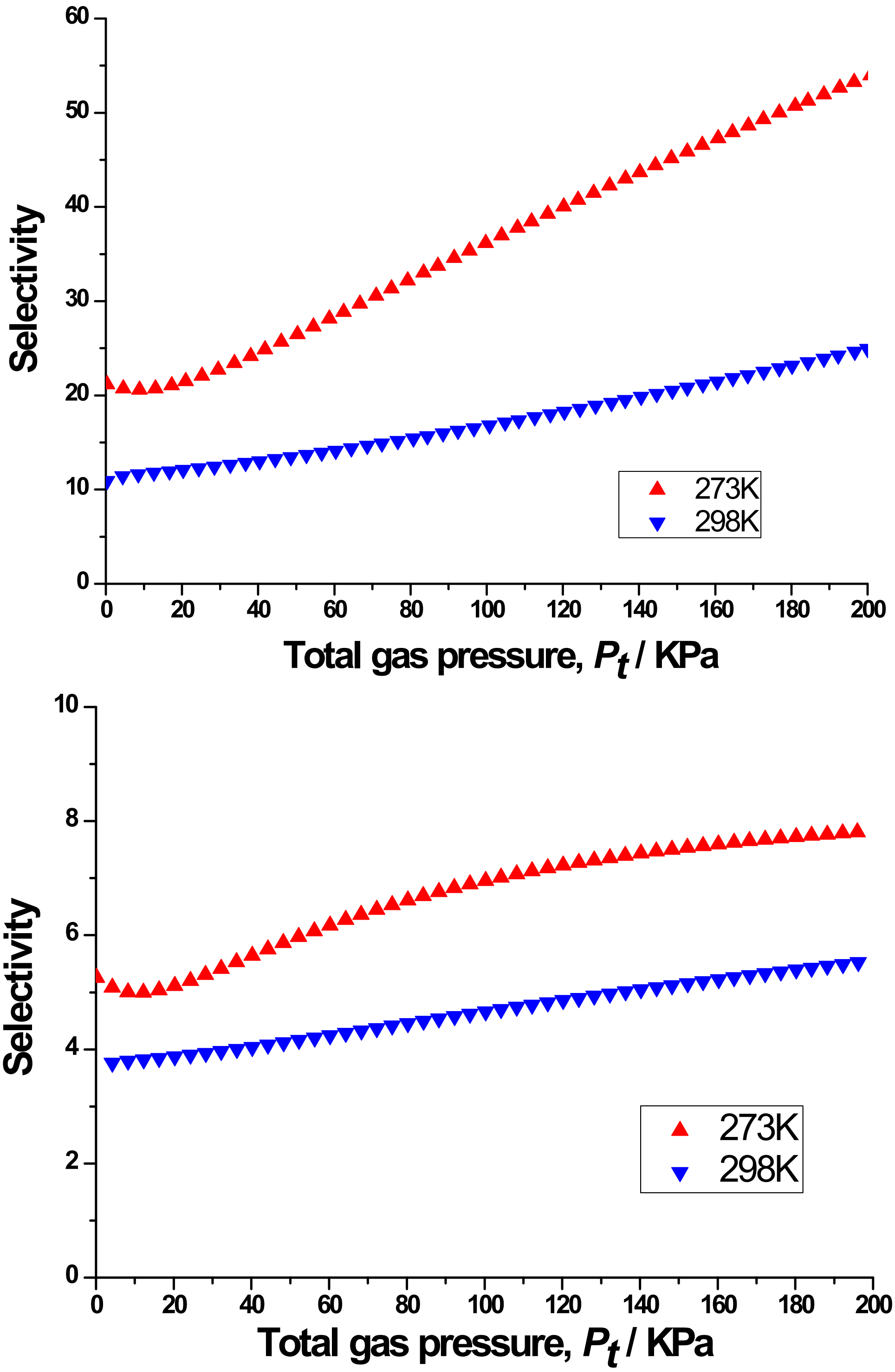

Fig. S20 Calculations of the adsorption selectivity, S_{ads}, using Ideal Adsorbed Solution Theory(IAST) for carbon dioxide/nitrogen (upper) and carbon dioxide/methane (lower) in CeBTC.

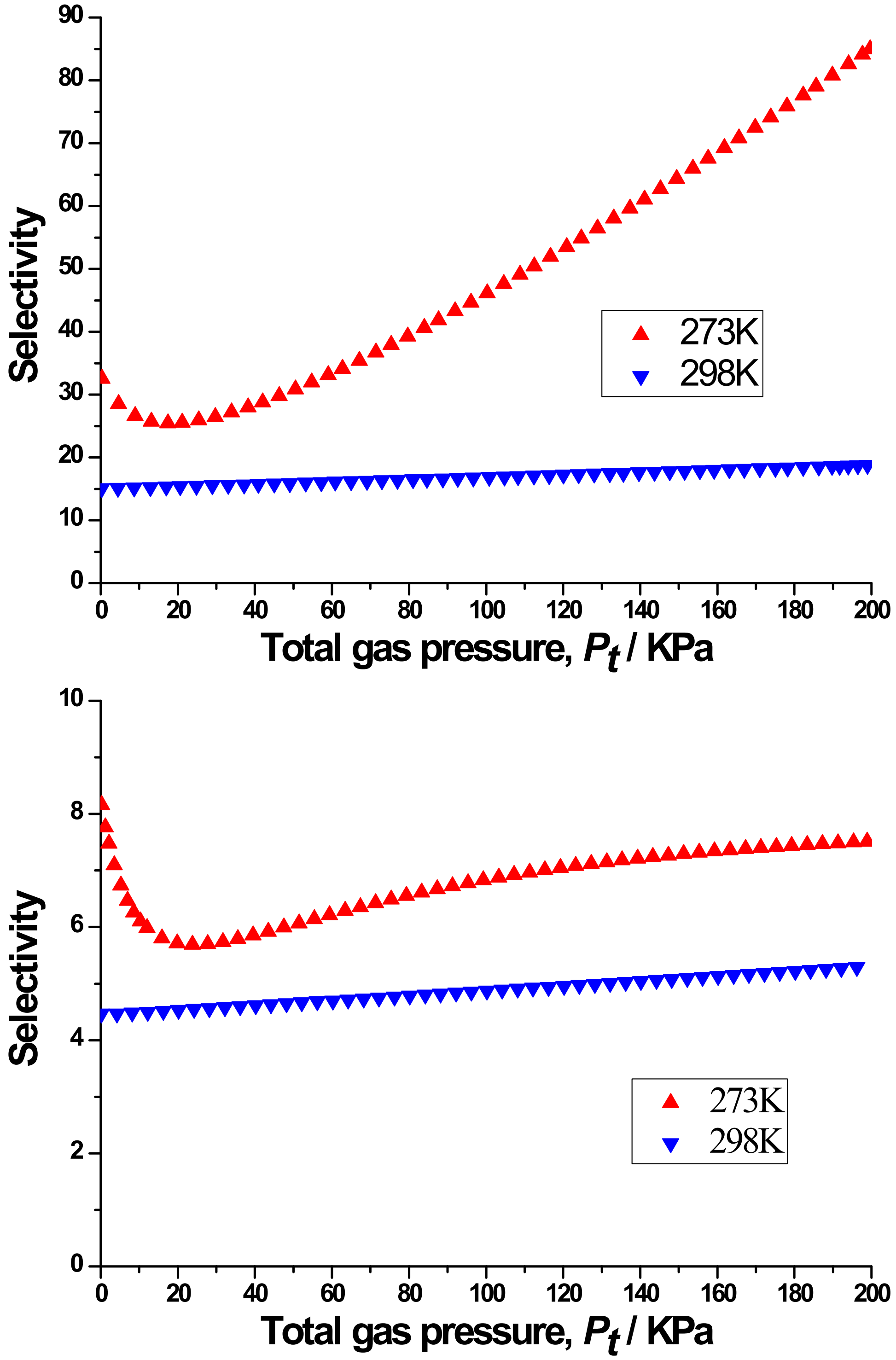

Fig. S21 Calculations of the adsorption selectivity, S_{ads}, using Ideal Adsorbed Solution Theory(IAST) for carbon dioxide/nitrogen (upper) and carbon dioxide/methane (lower) in PrBTC.

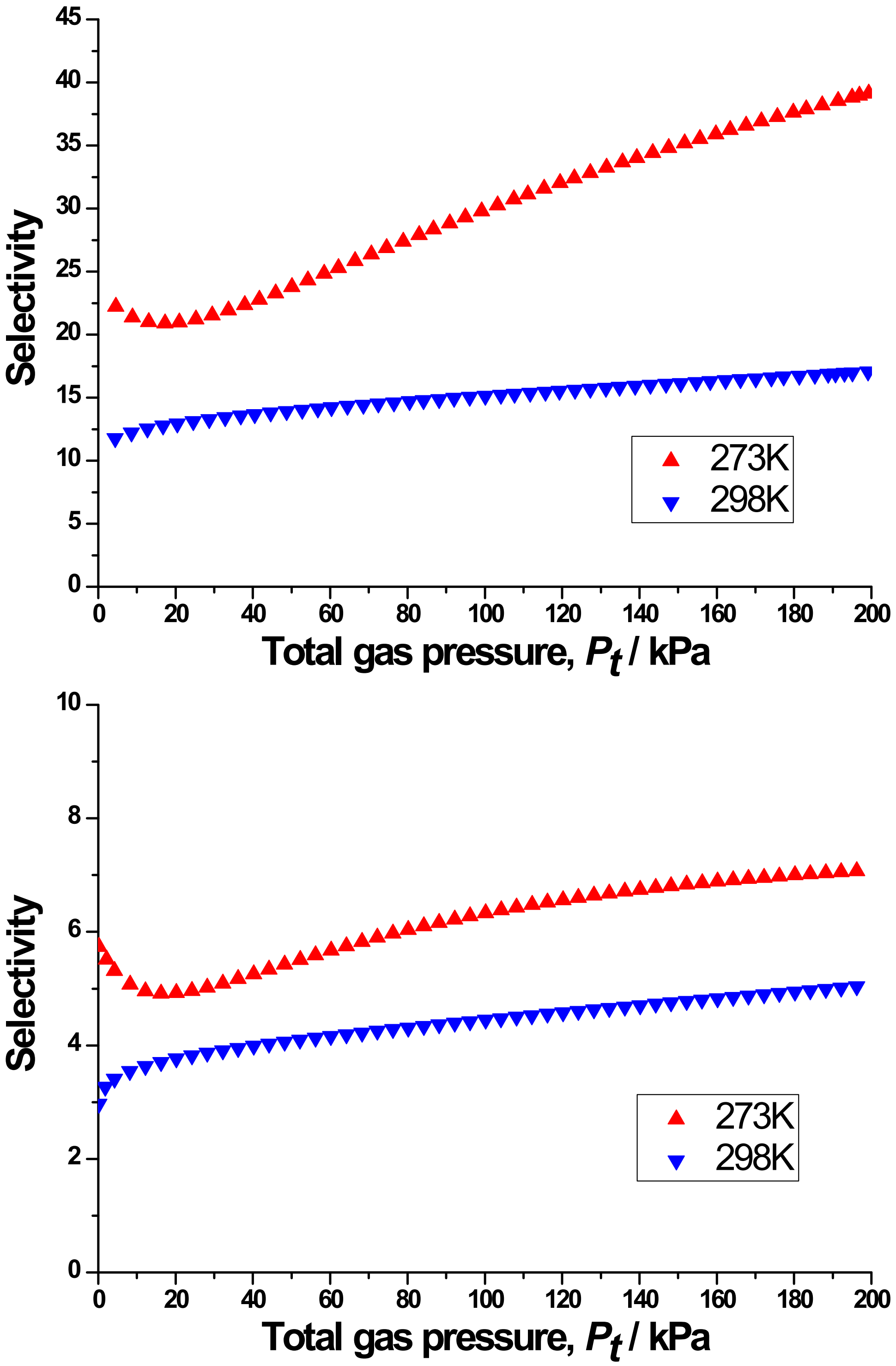

Fig. S22 Calculations of the adsorption selectivity, S_{ads}, using Ideal Adsorbed Solution Theory(IAST) for carbon dioxide/nitrogen (upper) and carbon dioxide/methane (lower) in NdBTC.

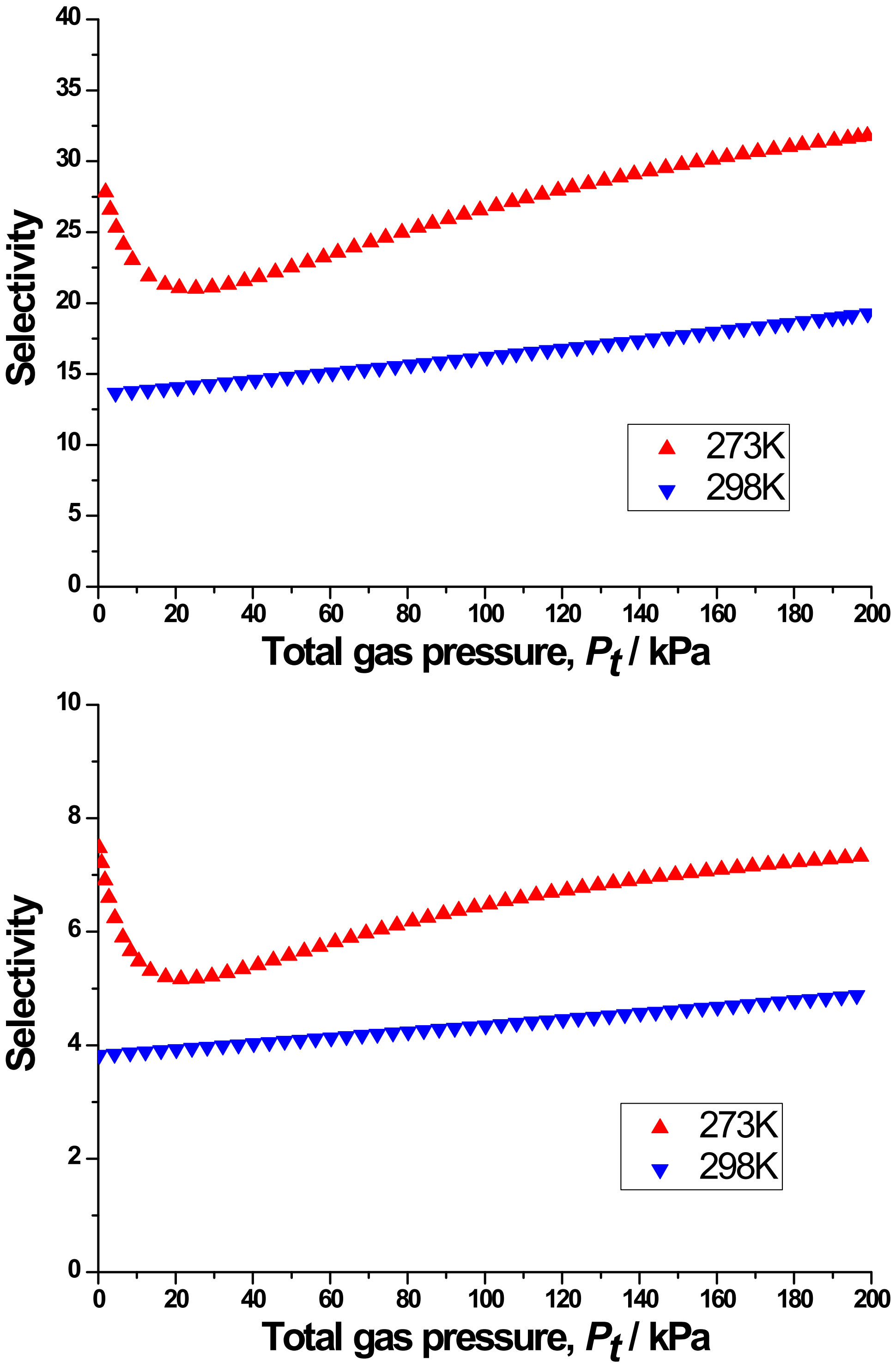

Fig. S23 Calculations of the adsorption selectivity, S_{ads}, using Ideal Adsorbed Solution Theory(IAST) for carbon dioxide/nitrogen (upper) and carbon dioxide/methane (lower) in SmBTC.

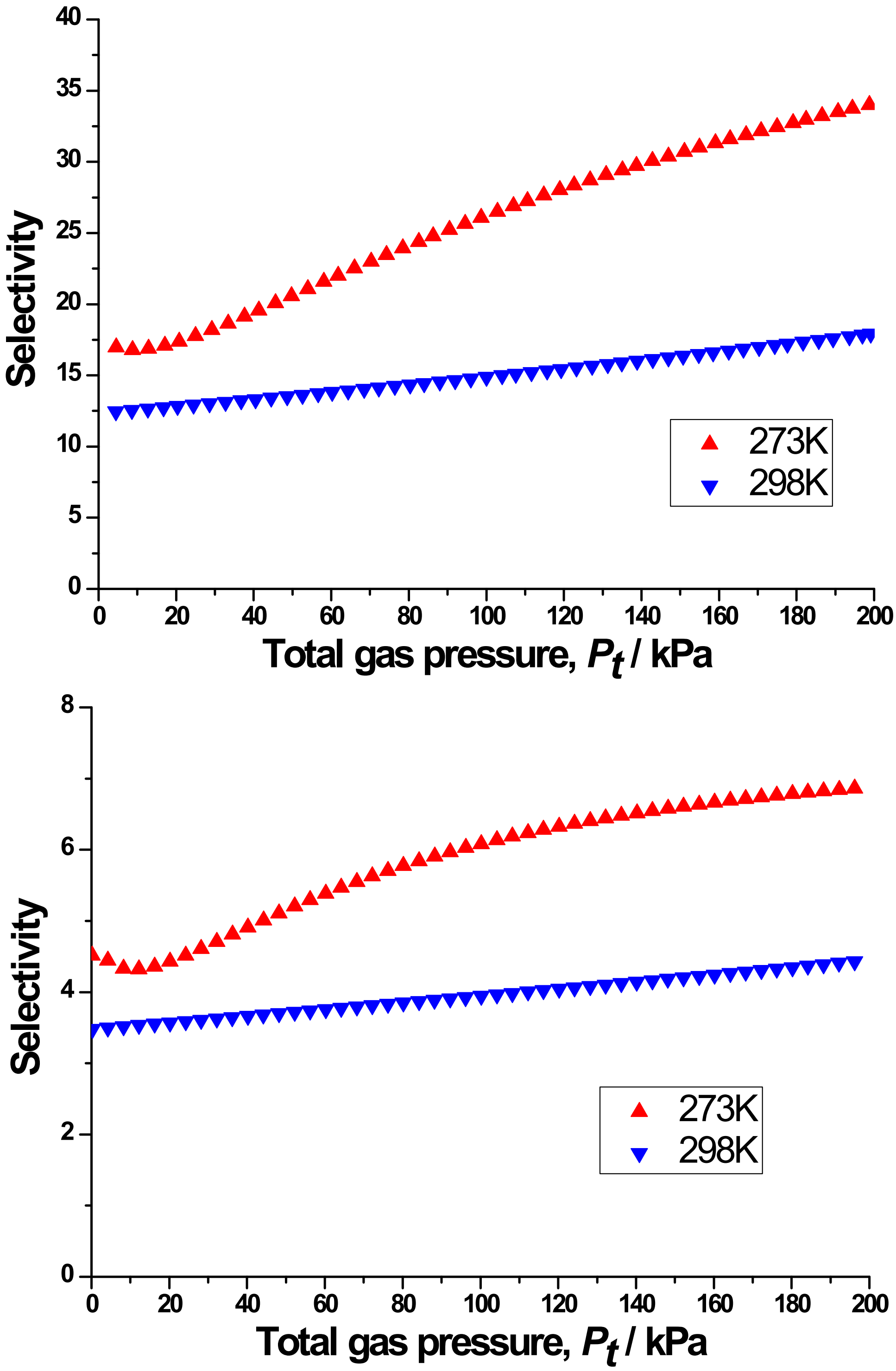

Fig. S24 Calculations of the adsorption selectivity, S_{ads}, using Ideal Adsorbed Solution Theory(IAST) for carbon dioxide/nitrogen (upper) and carbon dioxide/methane (lower) in EuBTC.

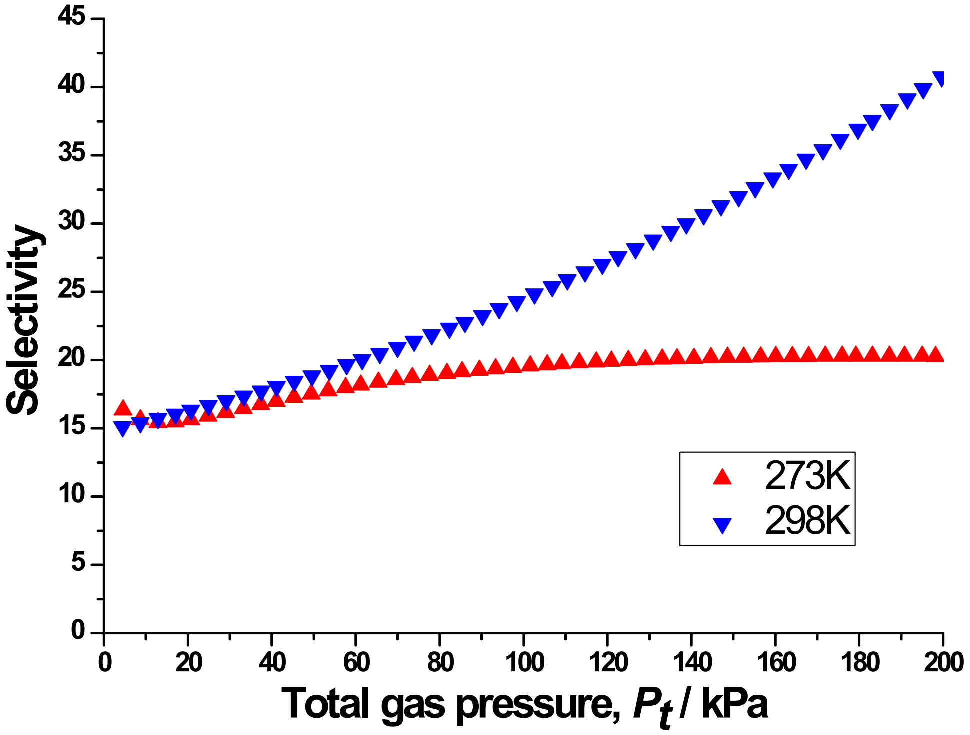

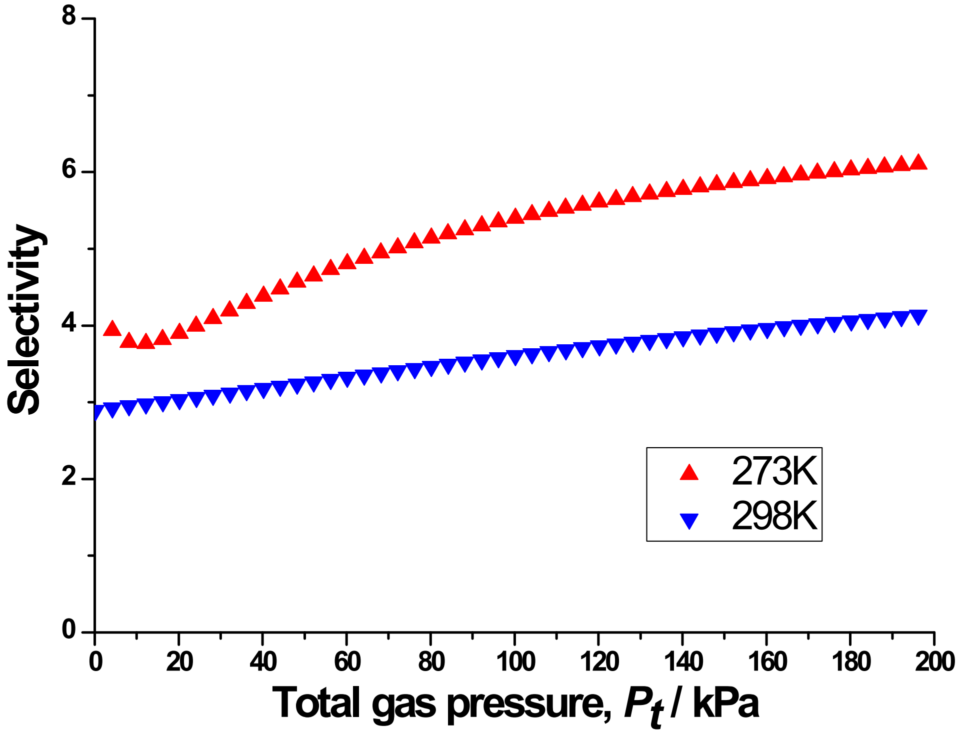

Fig. S25 Calculations of the adsorption selectivity, S_{ads}, using Ideal Adsorbed Solution Theory(IAST) for carbon dioxide/nitrogen (upper) and carbon dioxide/methane (lower) in GdBTC.

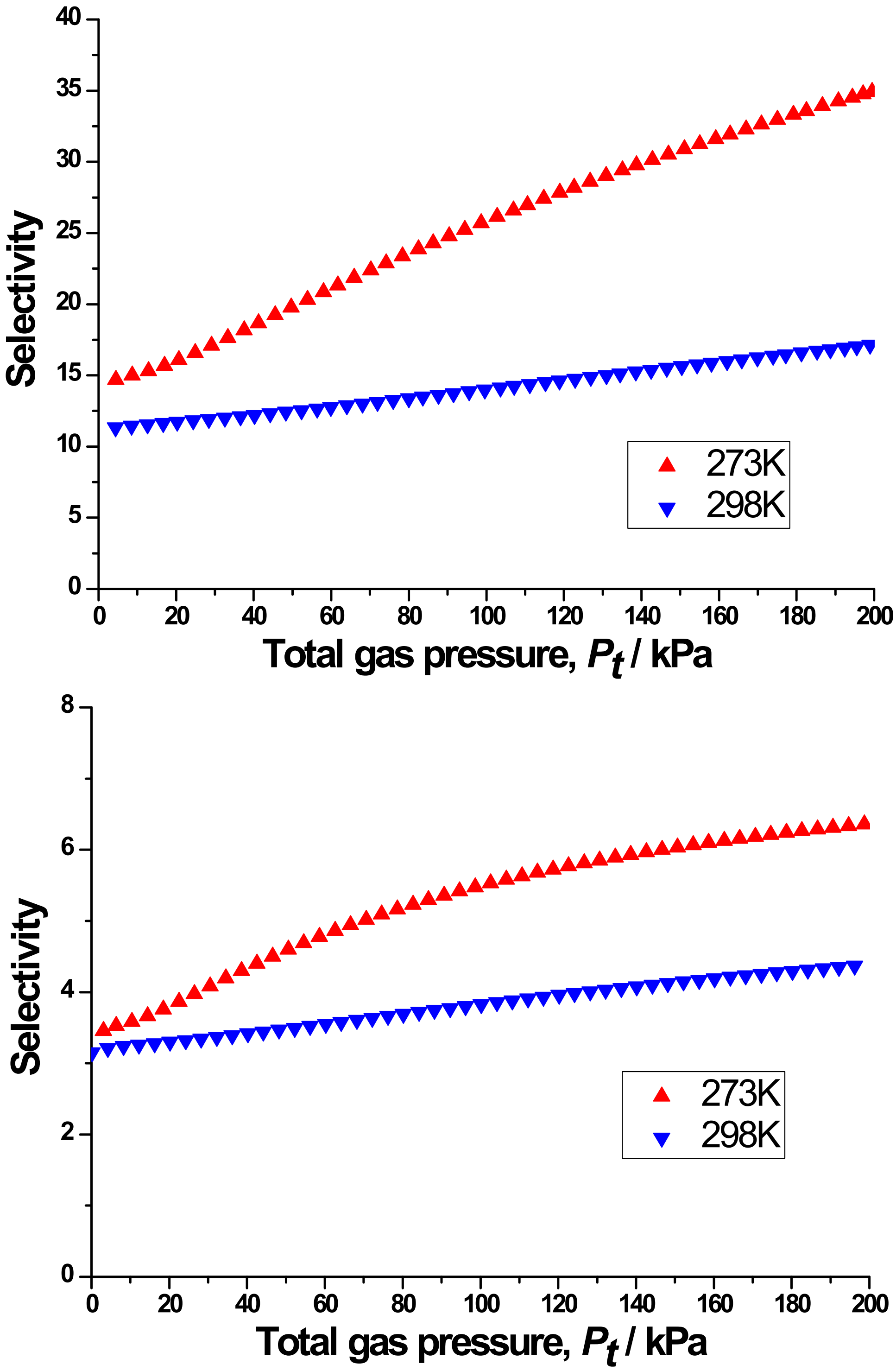

Fig. S26 Calculations of the adsorption selectivity, S_{ads}, using Ideal Adsorbed Solution Theory(IAST) for carbon dioxide/nitrogen (upper) and carbon dioxide/methane (lower) in TbBTC.

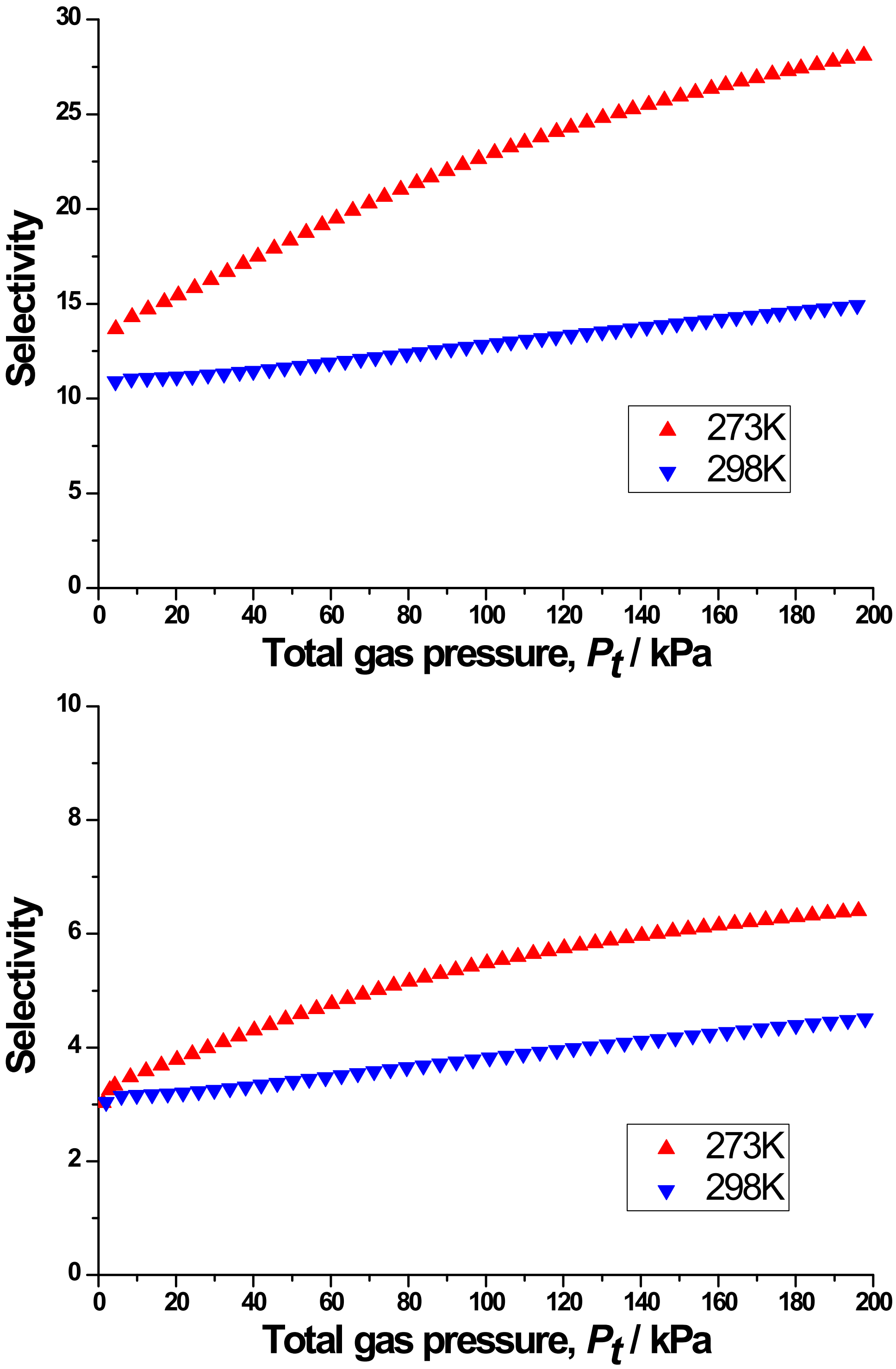

Fig. S27 Calculations of the adsorption selectivity, S_{ads}, using Ideal Adsorbed Solution Theory(IAST) for carbon dioxide/nitrogen (upper) and carbon dioxide/methane (lower) in DyBTC.

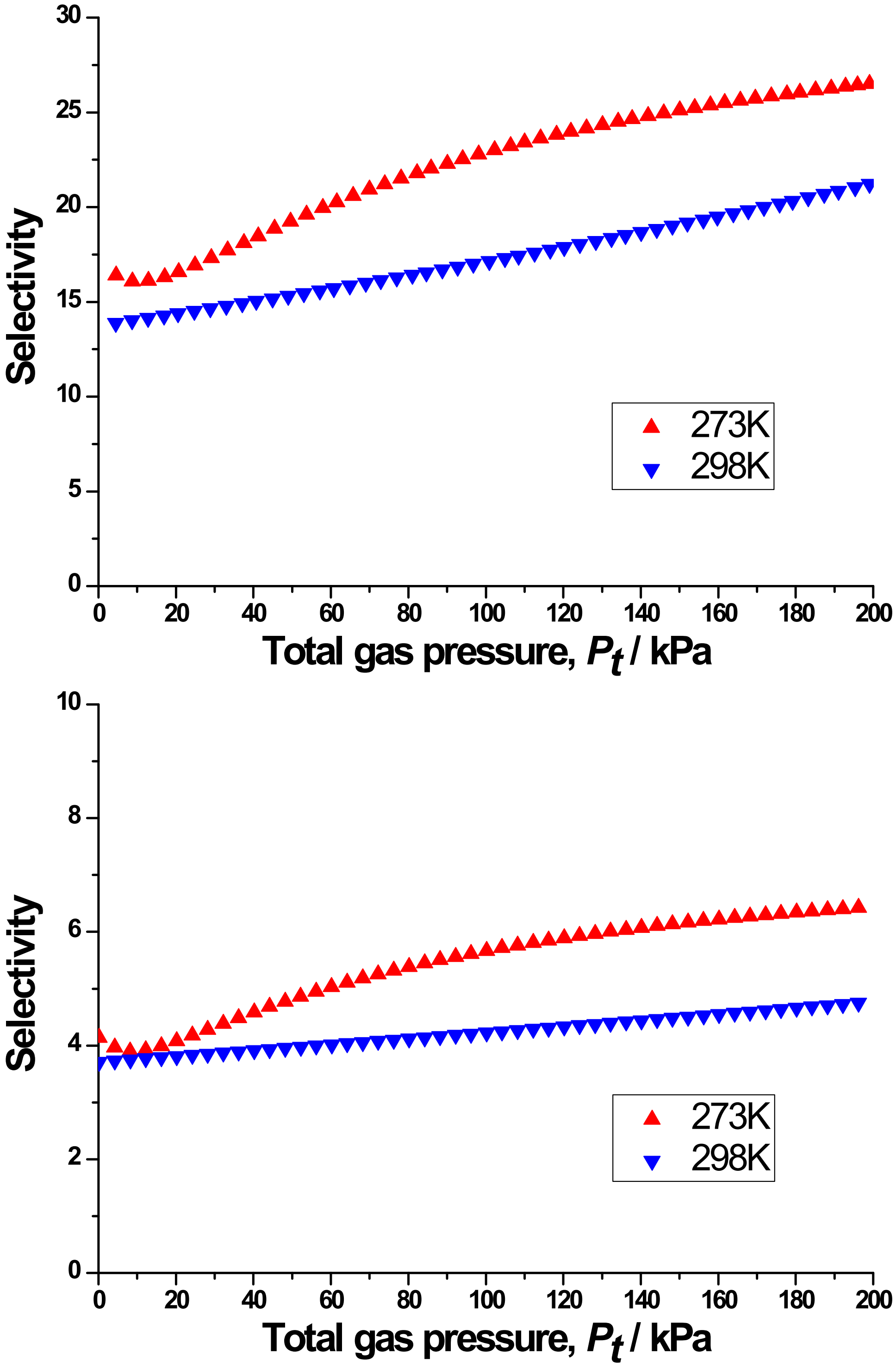

Fig. S28 Calculations of the adsorption selectivity, S_{ads}, using Ideal Adsorbed Solution Theory(IAST) for carbon dioxide/nitrogen (upper) and carbon dioxide/methane (lower) in HoBTC.

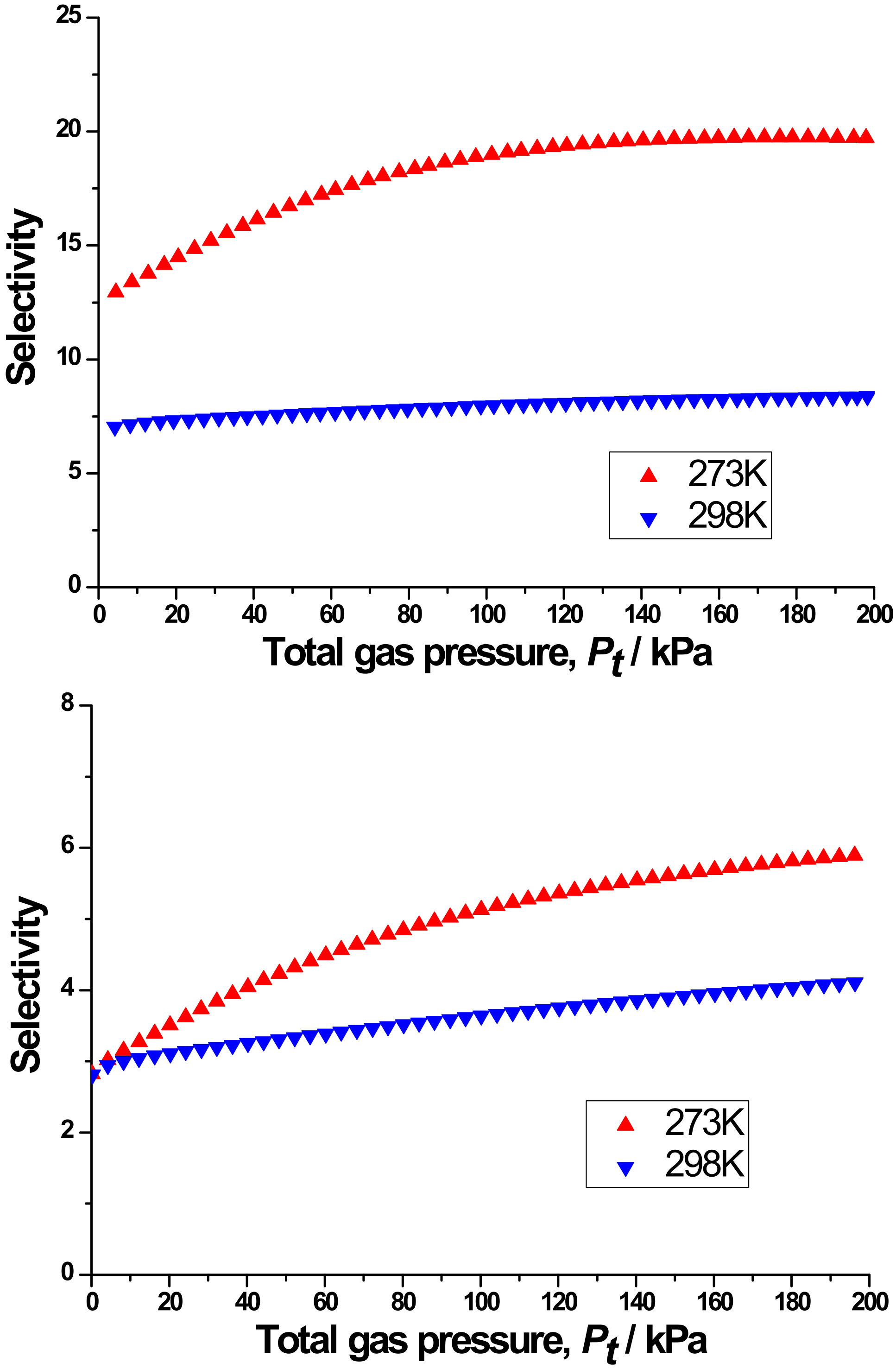

Fig. S29 Calculations of the adsorption selectivity, S_{ads}, using Ideal Adsorbed Solution Theory(IAST) for carbon dioxide/nitrogen (upper) and carbon dioxide/methane (lower) in ErBTC.

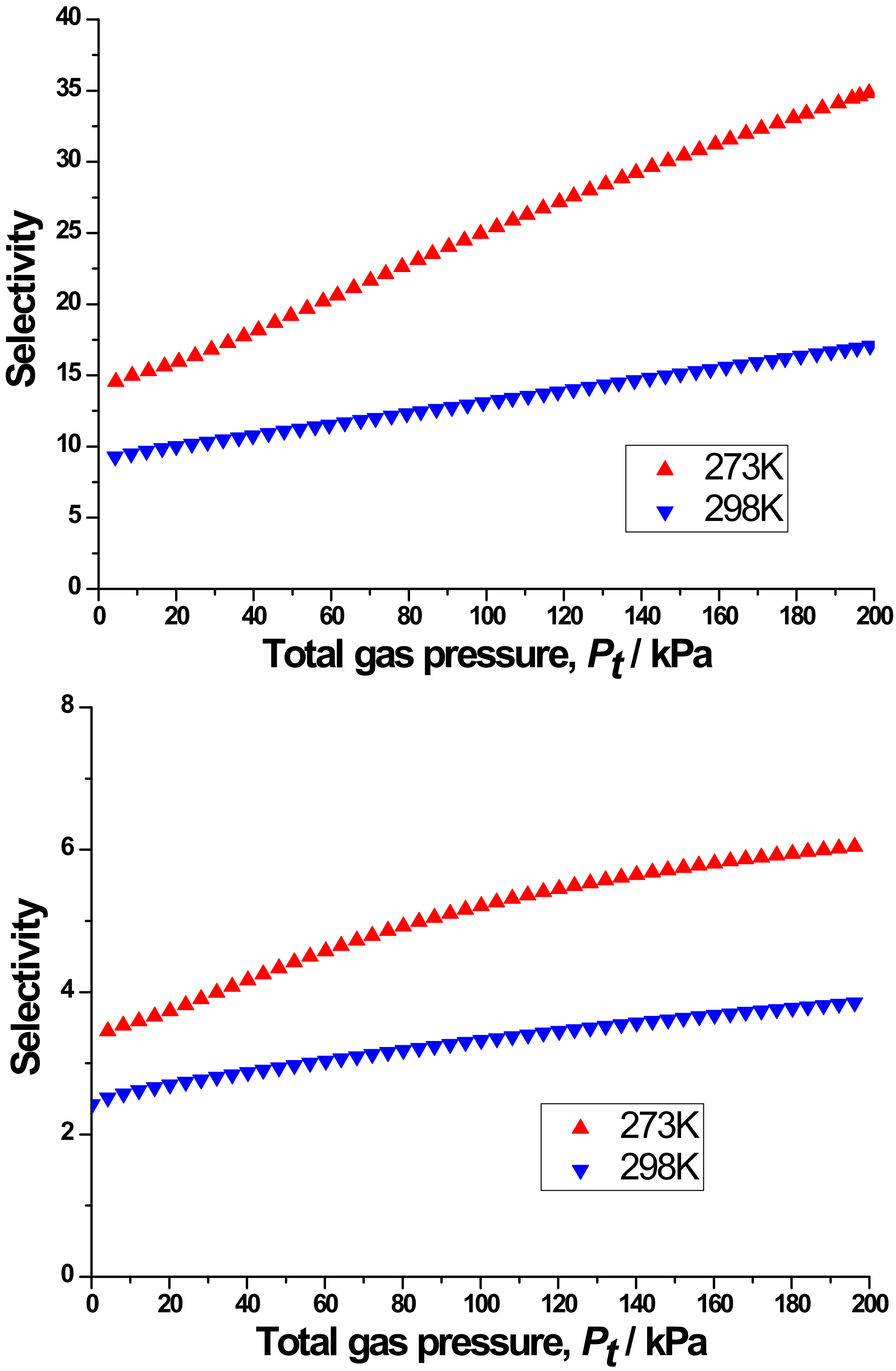

Fig. S30 Calculations of the adsorption selectivity, S_{ads}, using Ideal Adsorbed Solution Theory(IAST) for carbon dioxide/nitrogen (upper) and carbon dioxide/methane (lower) in TmBTC.

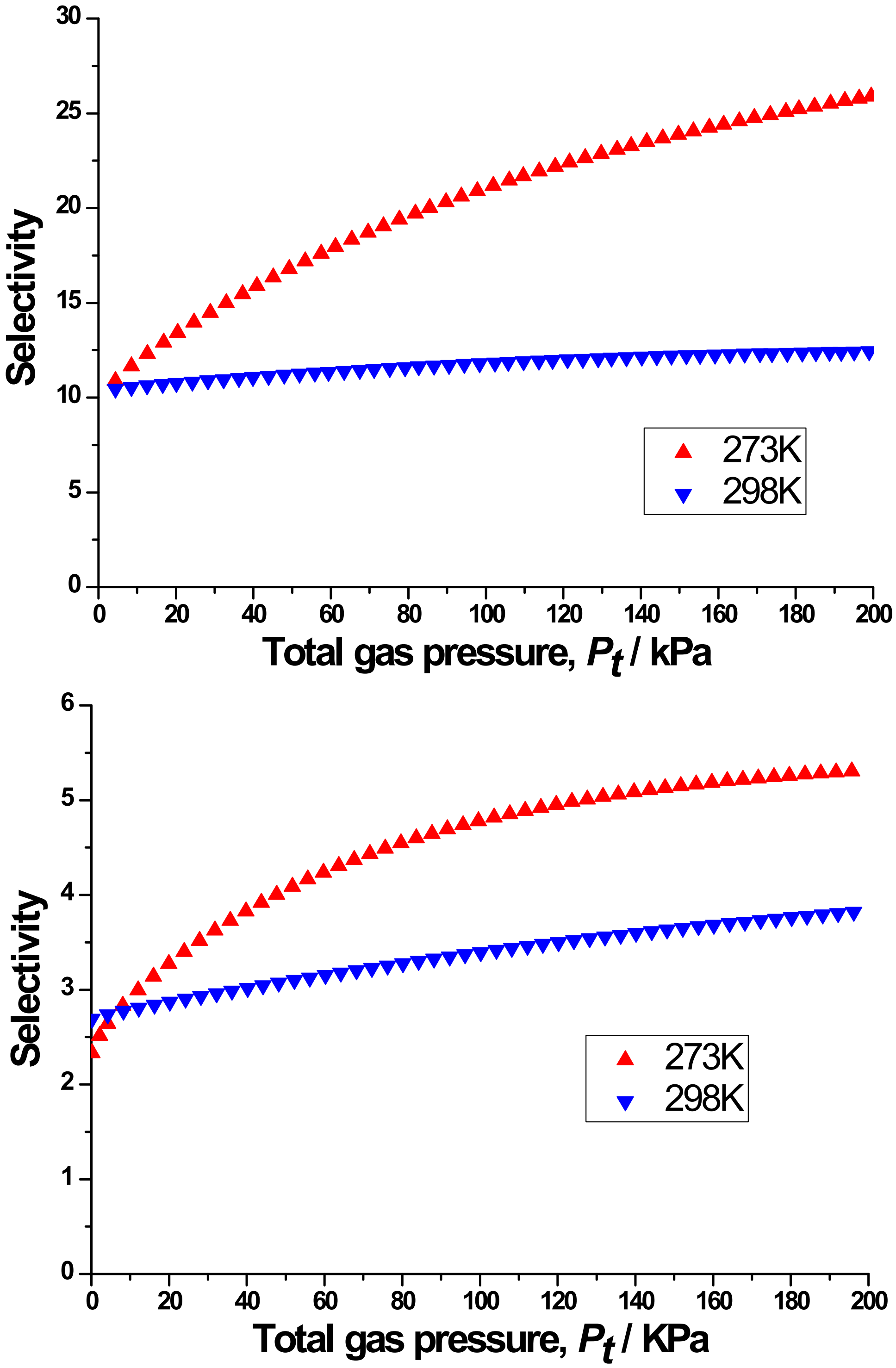

Fig. S31 Calculations of the adsorption selectivity, S_{ads}, using Ideal Adsorbed Solution Theory(IAST) for carbon dioxide/nitrogen (upper) and carbon dioxide/methane (lower) in YbBTC.

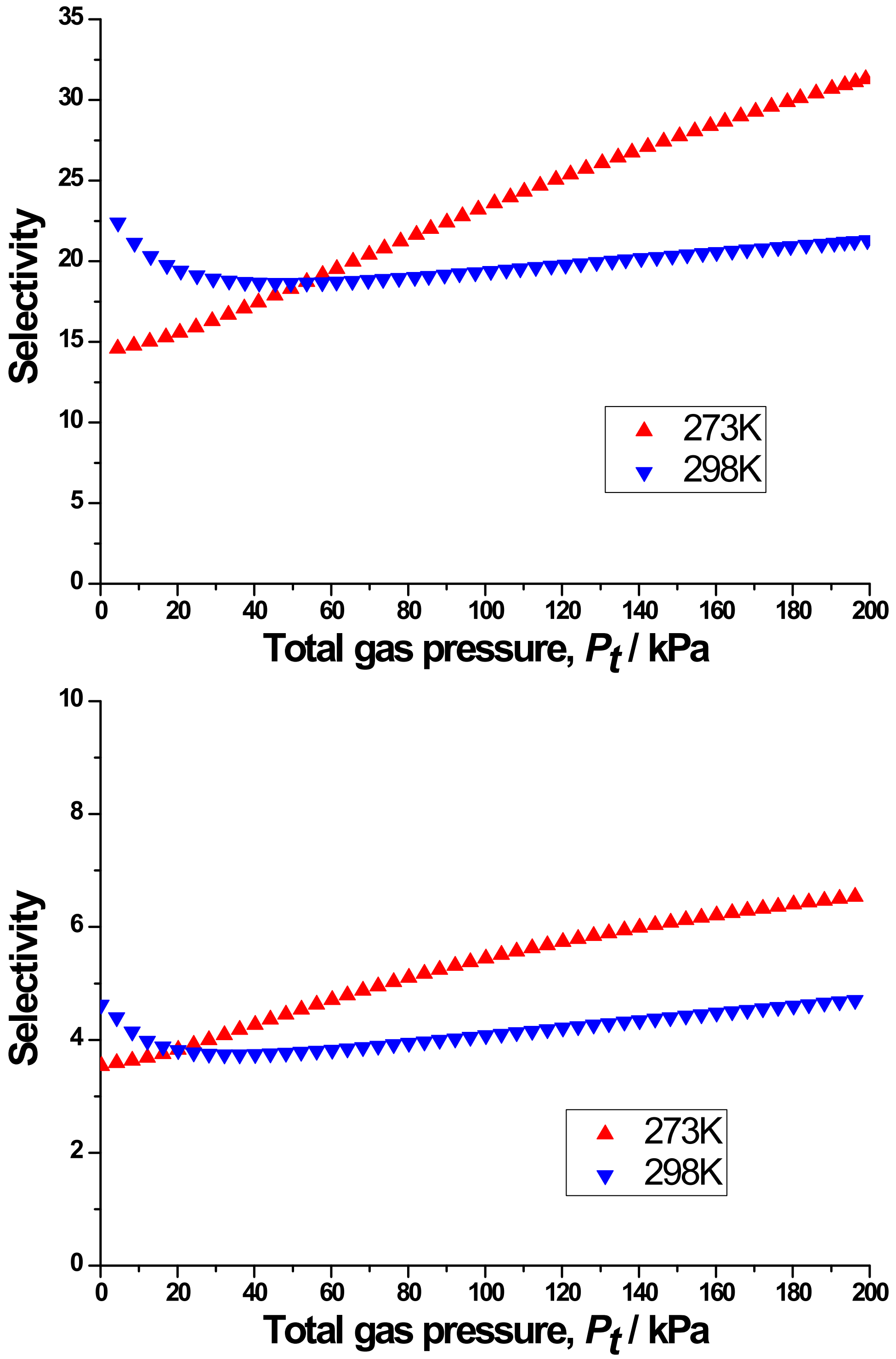

Fig. S32 Calculations of the adsorption selectivity, S_{ads}, using Ideal Adsorbed Solution Theory(IAST) for carbon dioxide/nitrogen (upper) and carbon dioxide/methane (lower) in YBTC.

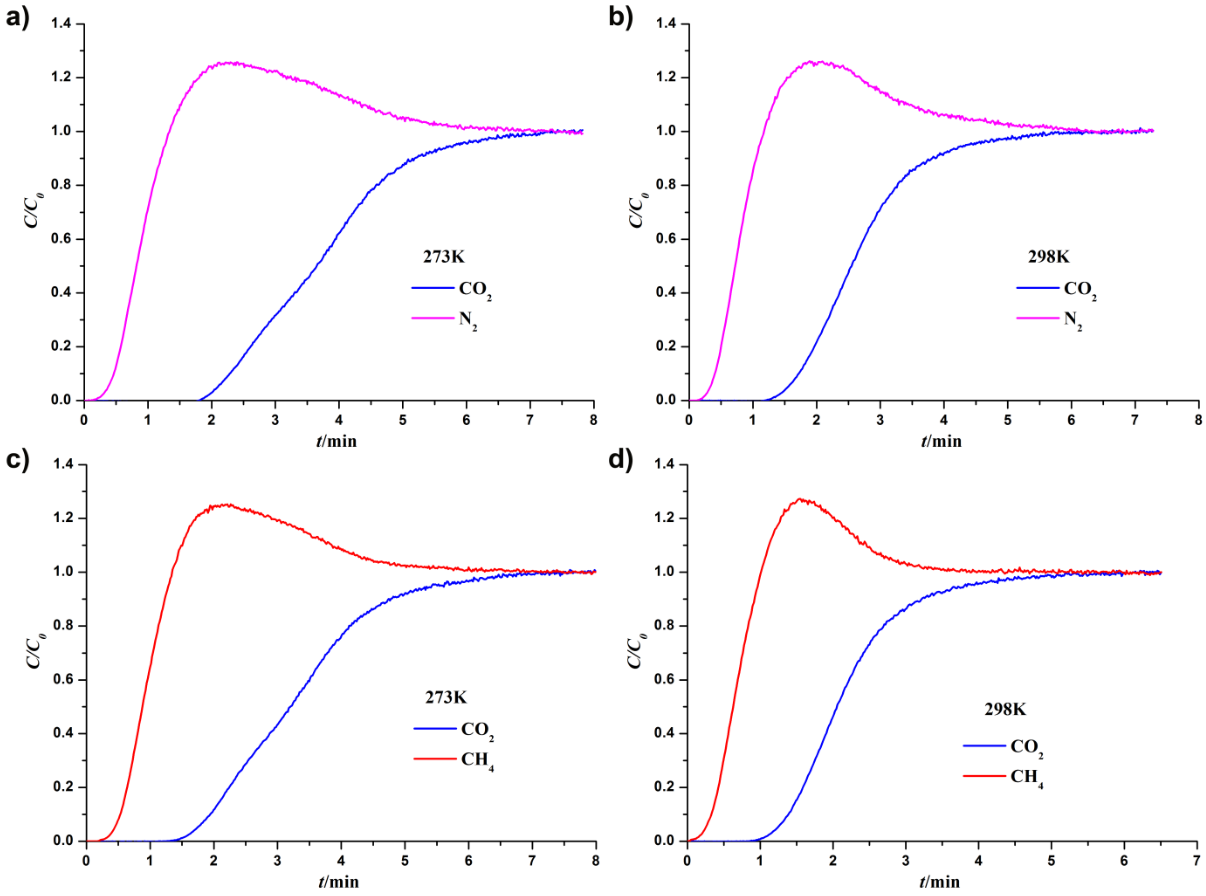

Fig. S33 Breakthrough curves of LaBTC: (a) CO_2/N_2 at 273K, (b) CO_2/N_2 at 298K, (c) CO_2/CH_4 at 273K, and (d) CO_2/CH_4 at 298K.

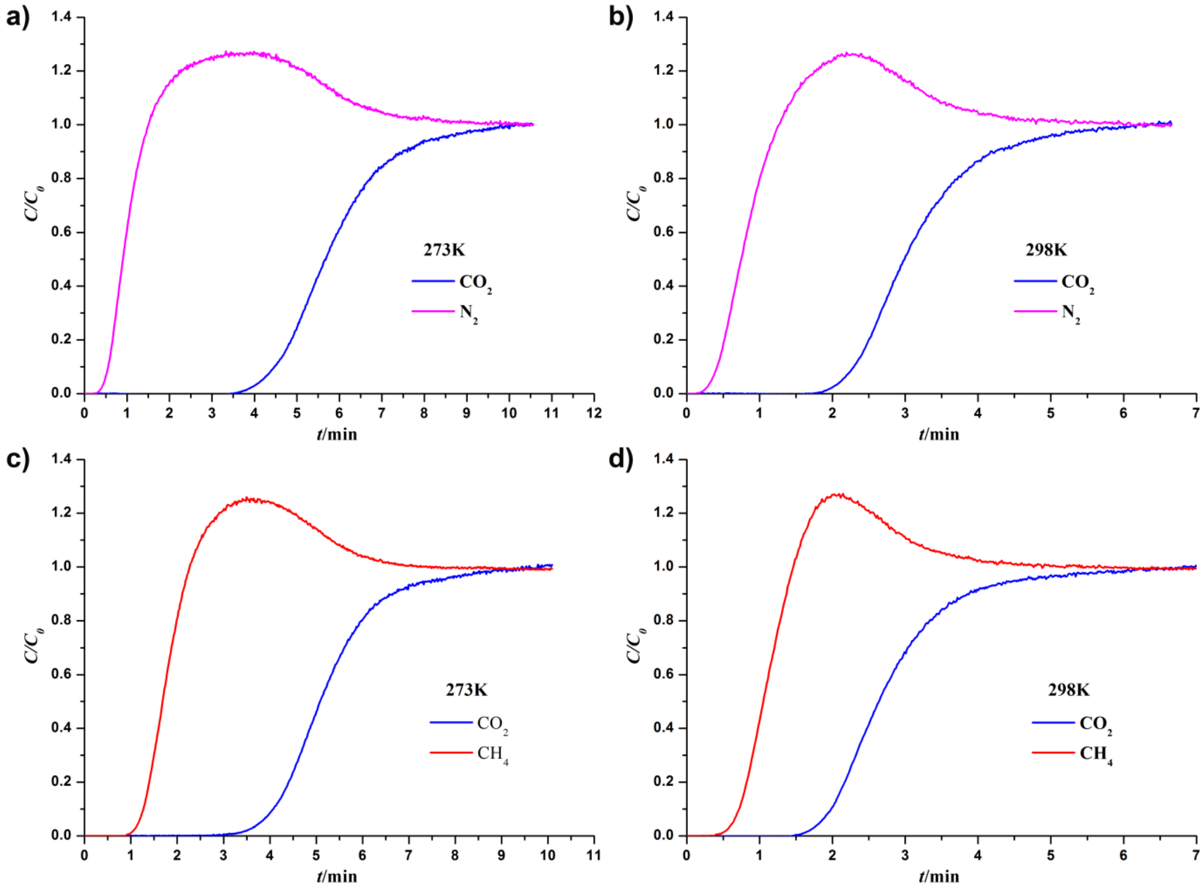

Fig. S34 Breakthrough curves of CeBTC: (a) CO_2/N_2 at 273K, (b) CO_2/N_2 at 298K, (c) CO_2/CH_4 at 273K, and (d) CO_2/CH_4 at 298K.

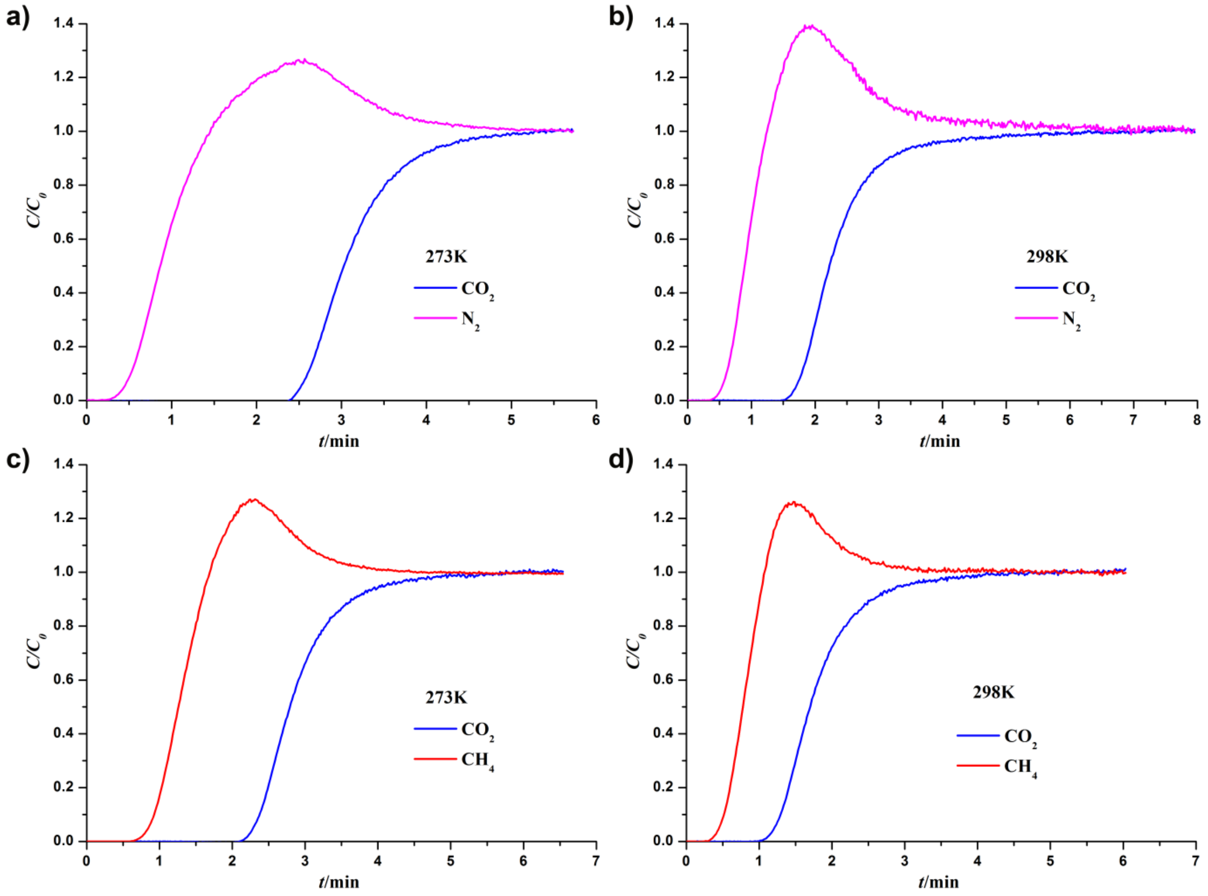

Fig. S35 Breakthrough curves of PrBTC: (a) CO_2/N_2 at 273K, (b) CO_2/N_2 at 298K, (c) CO_2/CH_4 at 273K, and (d) CO_2/CH_4 at 298K.

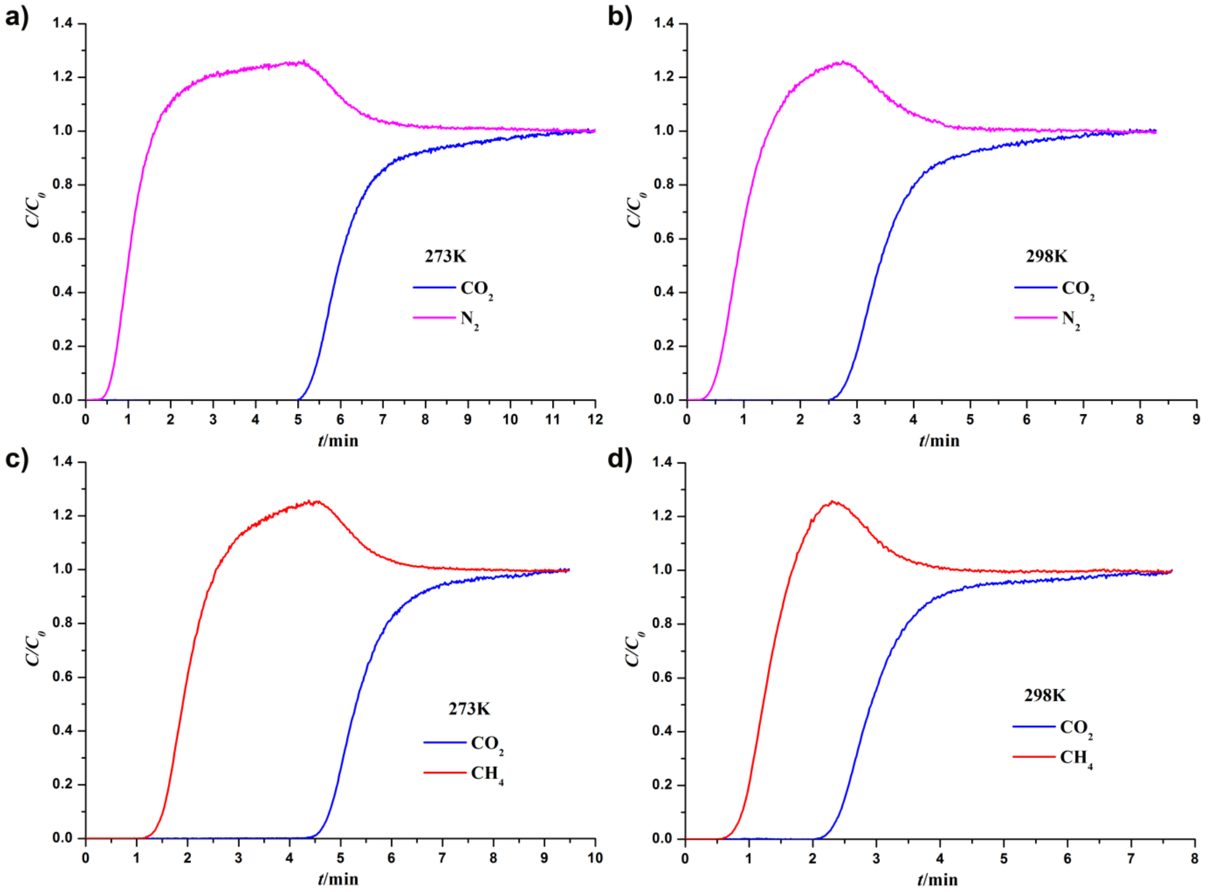

Fig. S36 Breakthrough curves of NdBTC: (a) CO_2/N_2 at 273K, (b) CO_2/N_2 at 298K, (c) CO_2/CH_4 at 273K, and (d) CO_2/CH_4 at 298K.

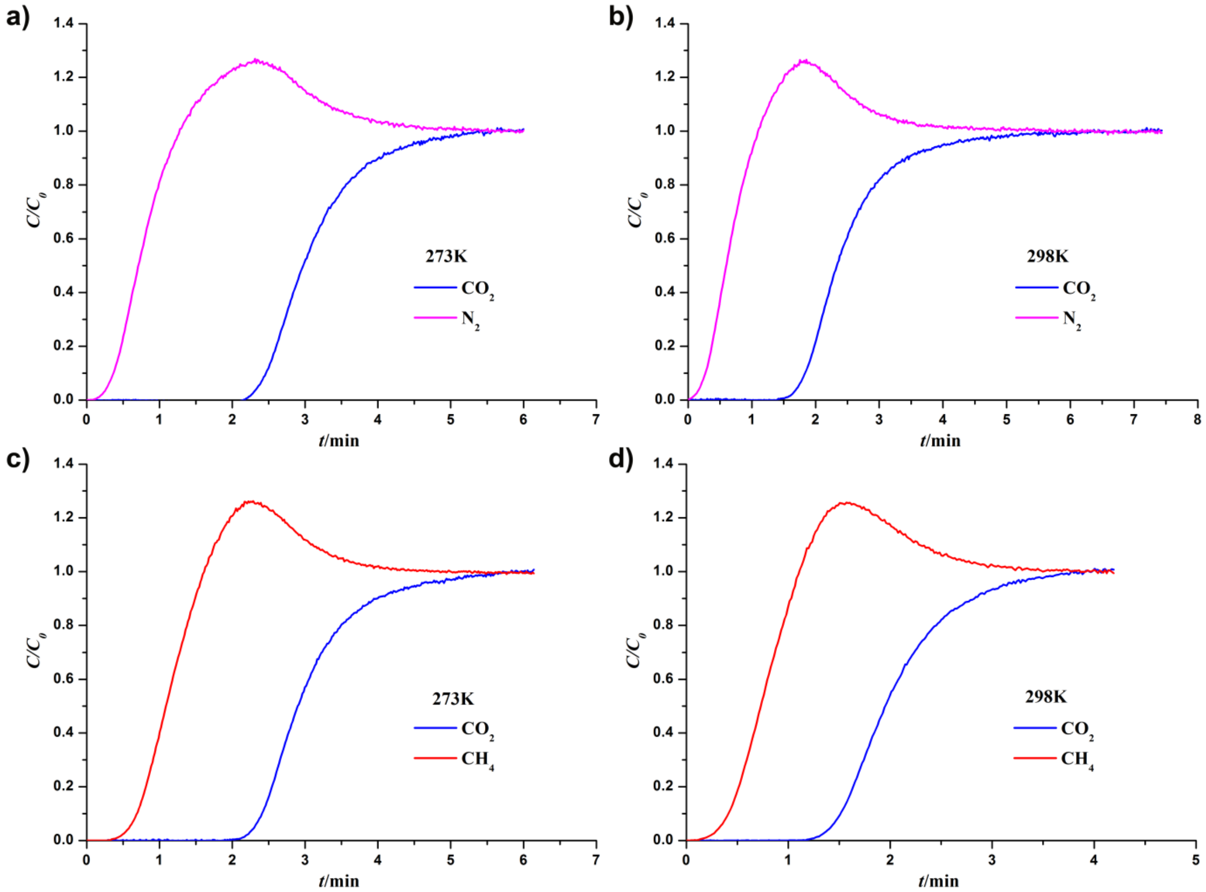

Fig. S37 Breakthrough curves of SmBTC: (a) CO_2/N_2 at 273K, (b) CO_2/N_2 at 298K, (c) CO_2/CH_4 at 273K, and (d) CO_2/CH_4 at 298K.

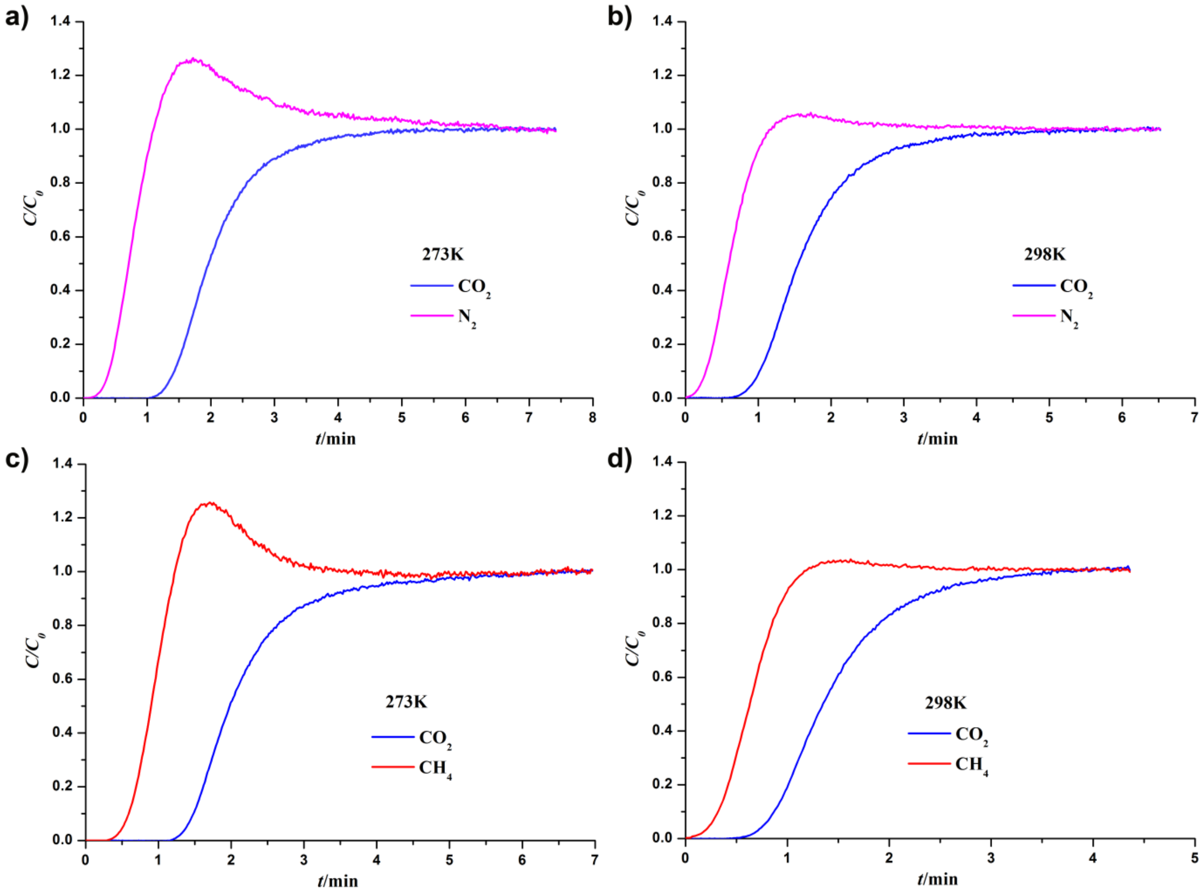

Fig. S38 Breakthrough curves of EuBTC: (a) CO_2/N_2 at 273K, (b) CO_2/N_2 at 298K, (c) CO_2/CH_4 at 273K, and (d) CO_2/CH_4 at 298K.

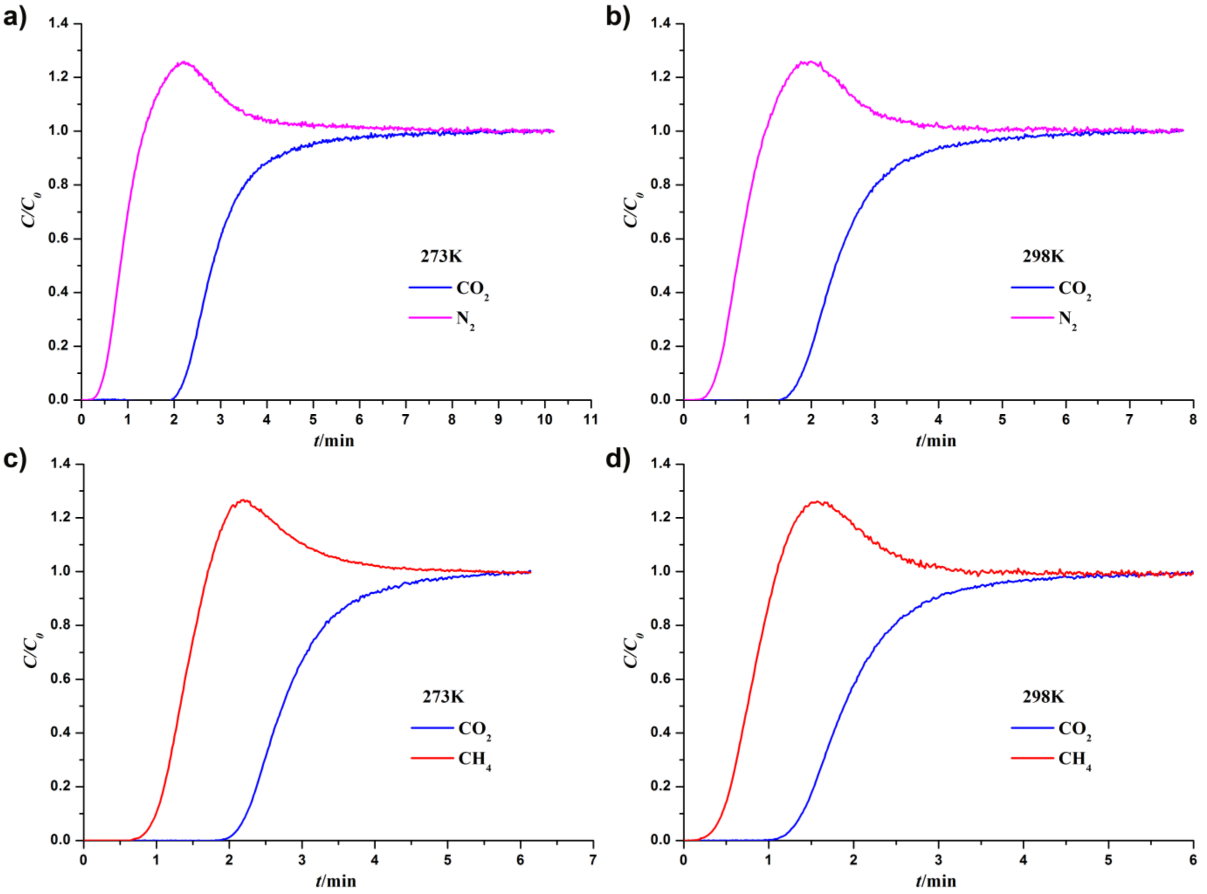

Fig. S39 Breakthrough curves of GdBTC: (a) CO_2/N_2 at 273K, (b) CO_2/N_2 at 298K, (c) CO_2/CH_4 at 273K, and (d) CO_2/CH_4 at 298K.

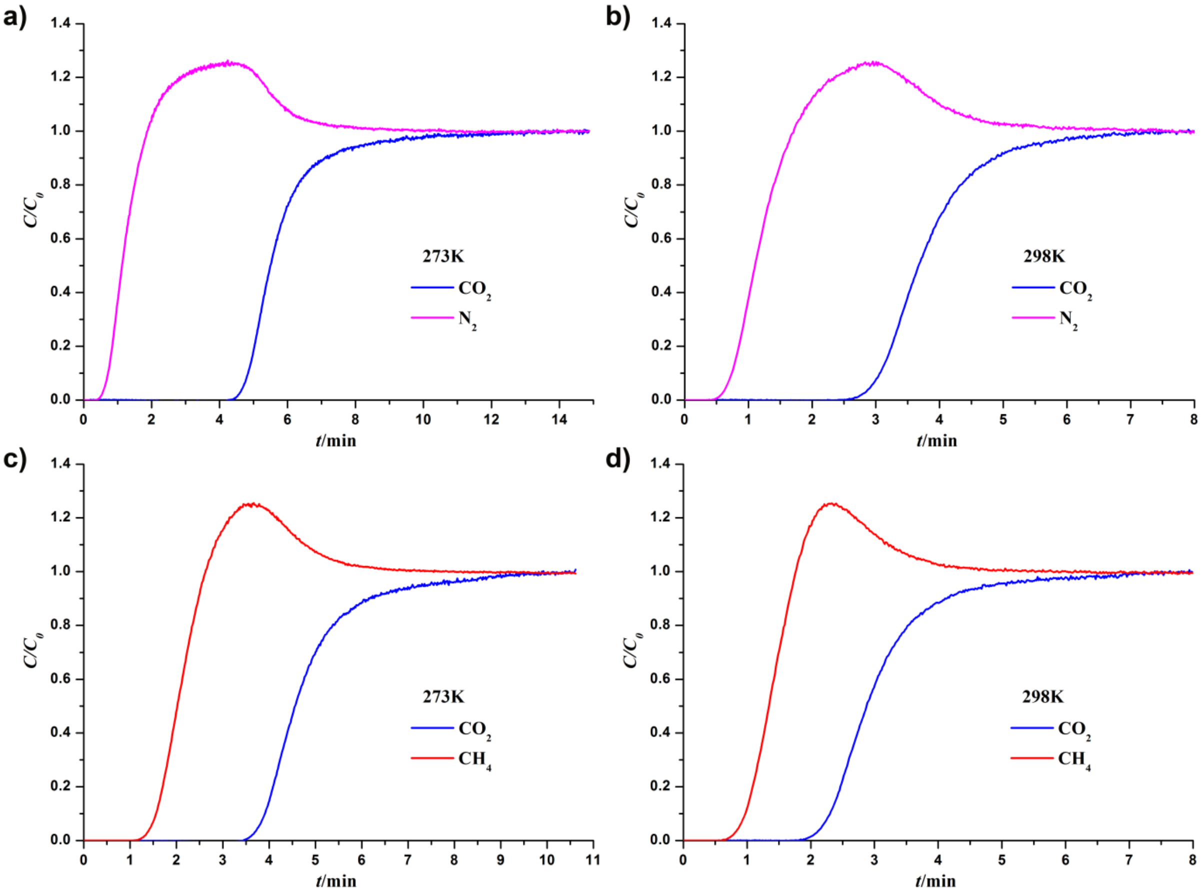

Fig. S40 Breakthrough curves of TbBTC: (a) CO_2/N_2 at 273K, (b) CO_2/N_2 at 298K, (c) CO_2/CH_4 at 273K, and (d) CO_2/CH_4 at 298K.

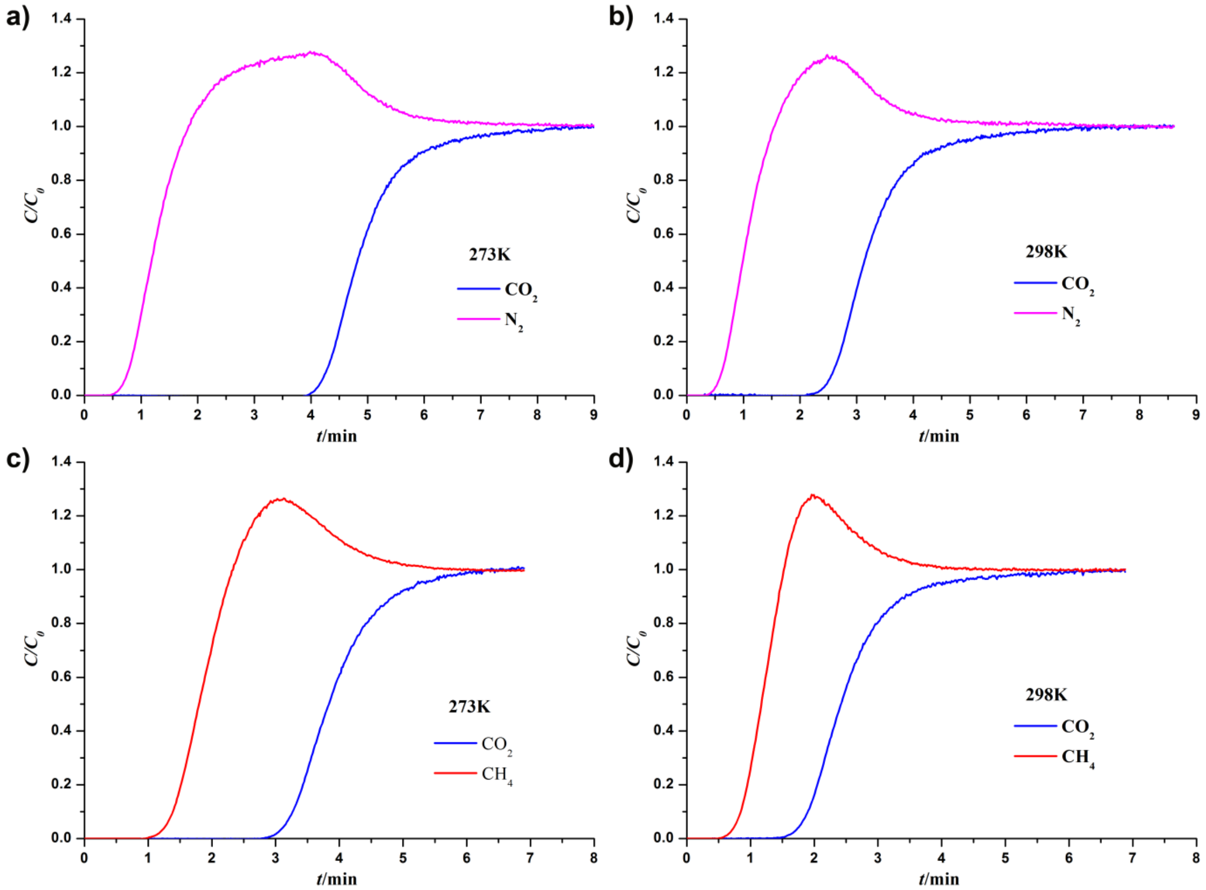

Fig. S41 Breakthrough curves of DyBTC: (a) CO_2/N_2 at 273K, (b) CO_2/N_2 at 298K, (c) CO_2/CH_4 at 273K, and (d) CO_2/CH_4 at 298K.

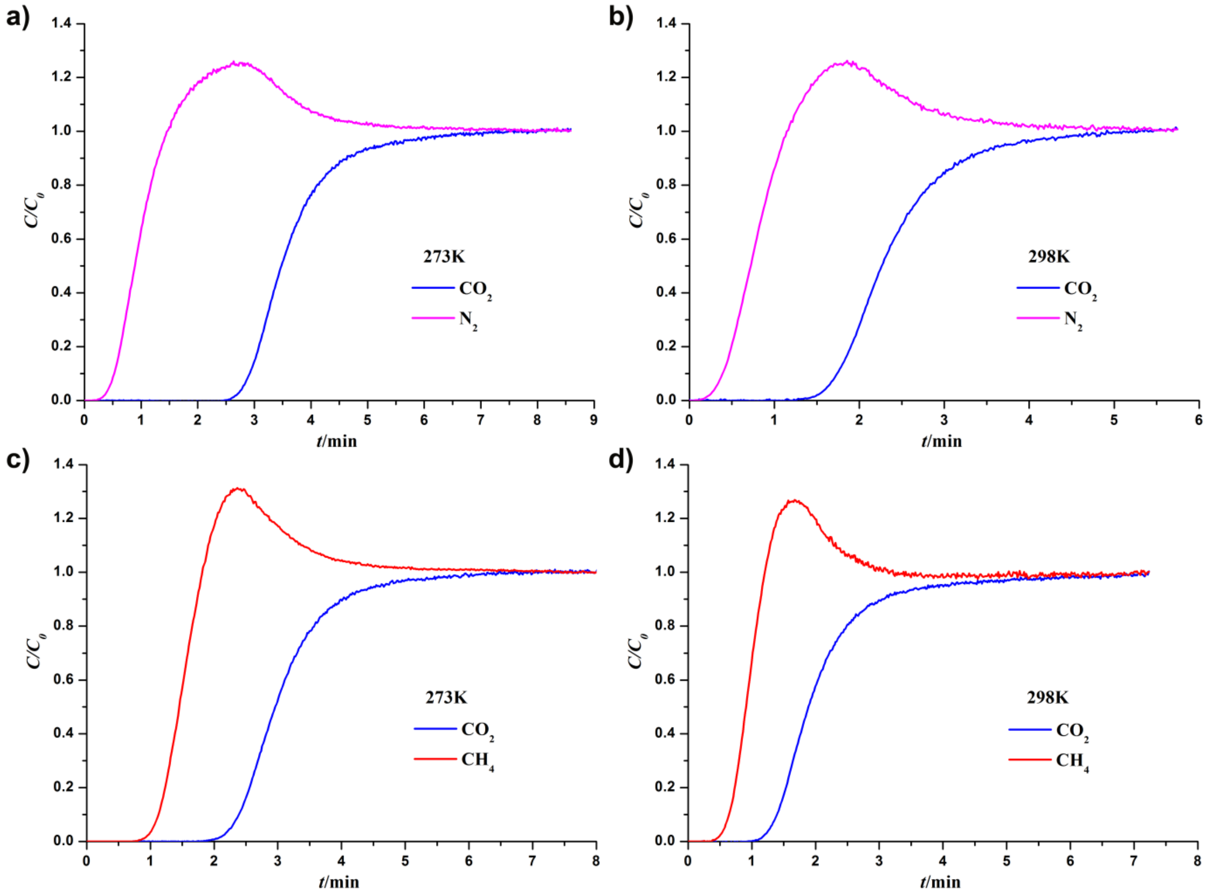

Fig. S42 Breakthrough curves of HoBTC: (a) CO_2/N_2 at 273K, (b) CO_2/N_2 at 298K, (c) CO_2/CH_4 at 273K, and (d) CO_2/CH_4 at 298K.

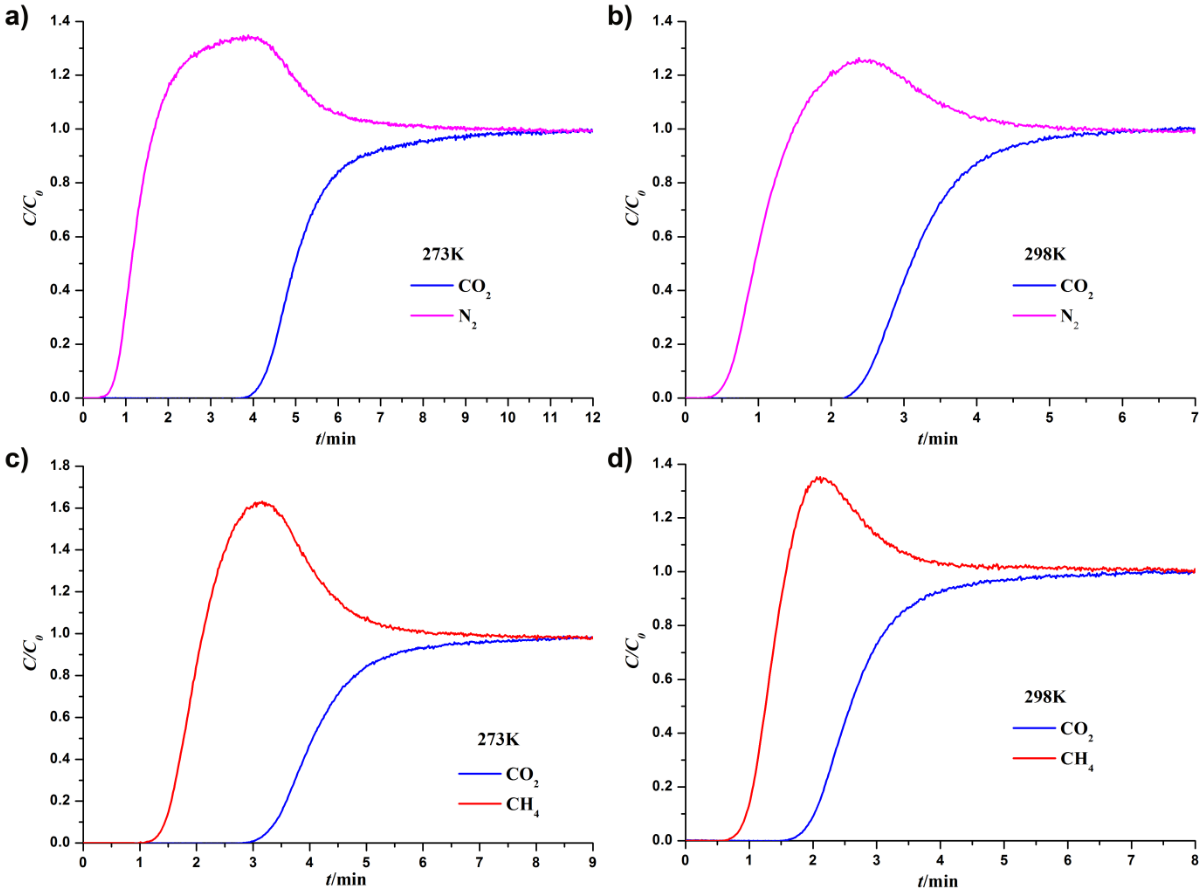

Fig. S43 Breakthrough curves of ErBTC: (a) CO_2/N_2 at 273K, (b) CO_2/N_2 at 298K, (c) CO_2/CH_4 at 273K, and (d) CO_2/CH_4 at 298K.

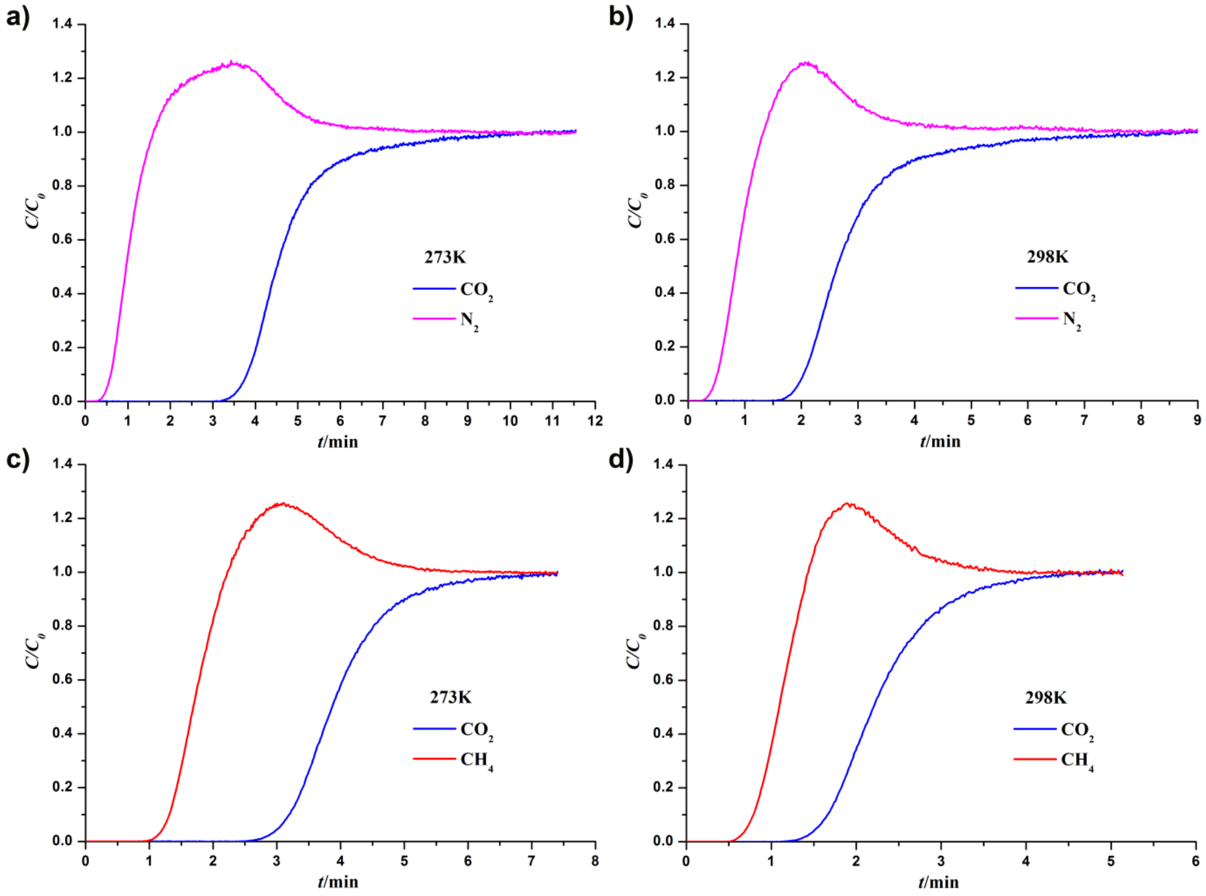

Fig. S44 Breakthrough curves of TmBTC: (a) CO_2/N_2 at 273K, (b) CO_2/N_2 at 298K, (c) CO_2/CH_4 at 273K, and (d) CO_2/CH_4 at 298K.

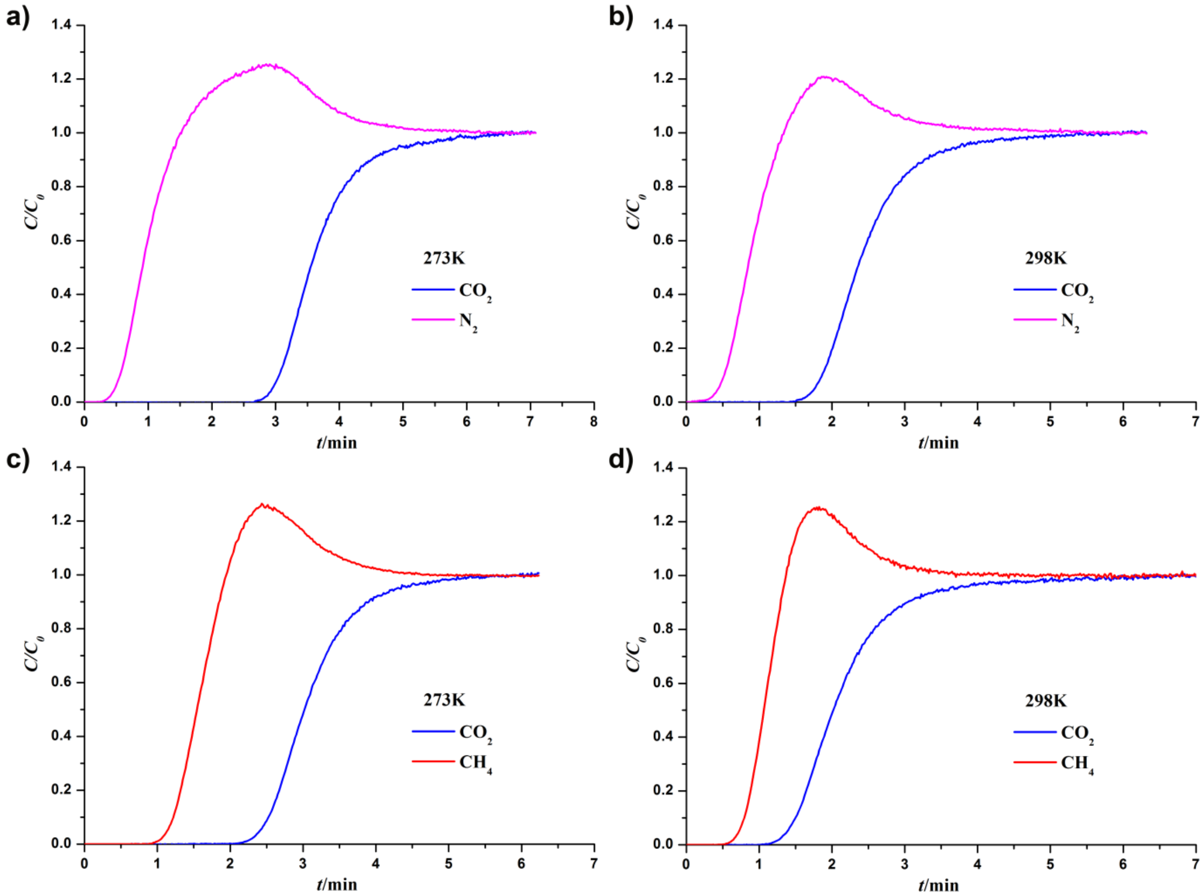

Fig. S45 Breakthrough curves of YbBTC: (a) CO_2/N_2 at 273K, (b) CO_2/N_2 at 298K, (c) CO_2/CH_4 at 273K, and (d) CO_2/CH_4 at 298K.

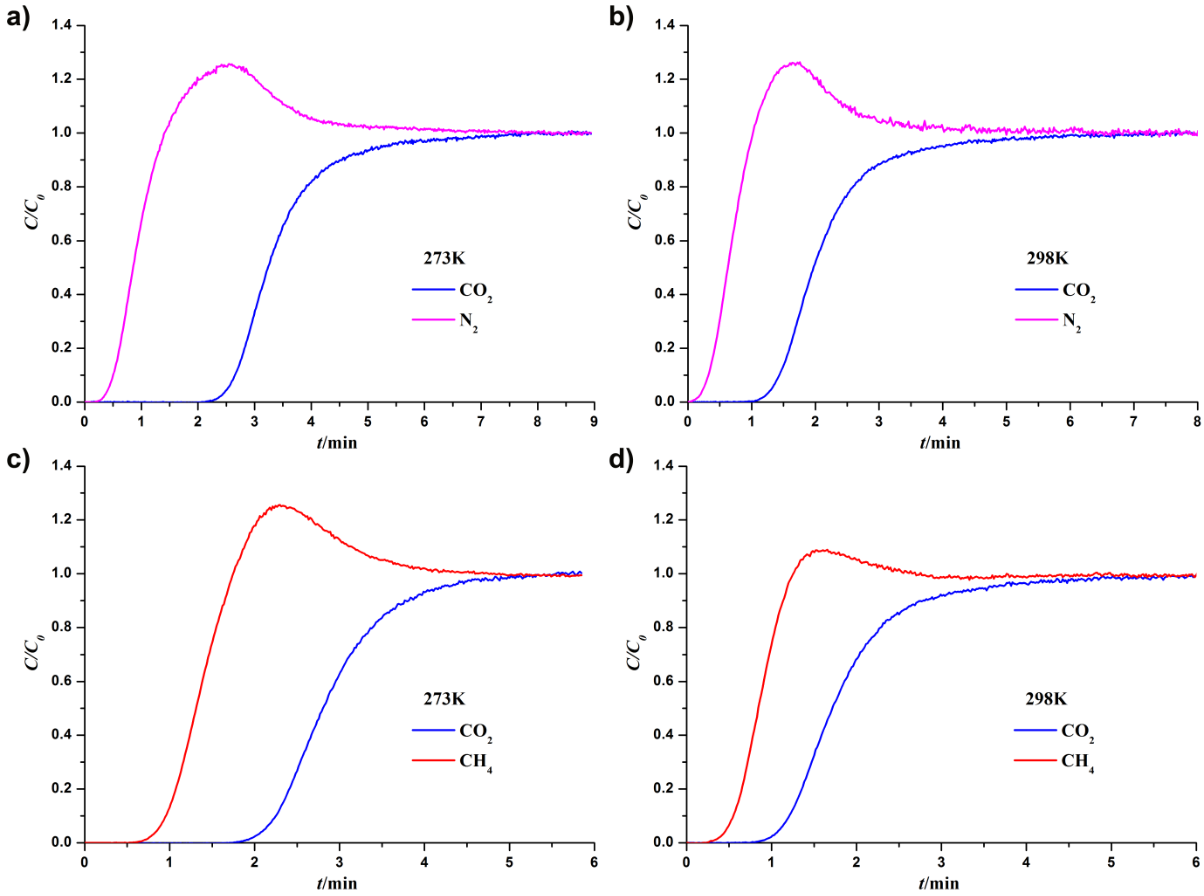

Fig. S46 Breakthrough curves of YBTC: (a) CO_2/N_2 at 273K, (b) CO_2/N_2 at 298K, (c) CO_2/CH_4 at 273K, and (d) CO_2/CH_4 at 298K.

Table S1 Ionic radii of Ln(III).

Ln(III)	**La**	**Ce**	**Pr**	**Nd**	**Sm**	**Eu**	**Gd**	**Tb**	**Dy**	**Ho**	**Er**	**Tm**	**Yb**	**Y**
Radius(pm)	103	102	99	98	96	95	94	92	91	90	89	88	87	90

Table S2 The pore parameters of as synthesized LOFs.

	Surface Area		Pore Volume	Pore Size
	Langmuir	BET	(cm^3 g^{-1})	(nm)
LaBTC	811.9	742.1	0.32	1.28
CeBTC	816.8	744.0	0.30	1.47
PrBTC	1114.4	969.5	0.41	1.12
NdBTC	931.8	828.3	0.34	1.18
SmBTC	815.0	740.1	0.30	1.12
EuBTC	817.1	771.2	0.30	1.12
GdBTC	882.4	836.3	0.32	1.12
TbBTC	842.5	803.3	0.30	1.12
DyBTC	868.5	806.4	0.31	1.12
HoBTC	786.0	725.5	0.28	1.48
ErBTC	795.0	709.0	0.29	1.54
TmBTC	840.7	747.6	0.30	1.12
YbBTC	947.6	910.3	0.35	1.11
YBTC	1159.6	1017.4	0.42	1.18

Table S3 Parameters for Dual-site Langmuir-Freundlich model $q_i = q_{i,A,sat}\frac{b_{i,A}p_i^{v_{i,A}}}{1+b_{i,A}p_i^{v_{i,A}}} + q_{i,B,sat}\frac{b_{i,B}p_i^{v_{i,B}}}{1+b_{i,B}p_i^{v_{i,B}}}$ adsorption of CO_2 in LaBTC at 273K and 298 K.

	Site A			Site B		
	$q_{\mathrm{i,A},sat}$	$b_{\mathrm{i,A}}$	$V_{\mathrm{i,A}}$	$q_{\mathrm{i,B},sat}$	$b_{\mathrm{i,B}}$	$V_{\mathrm{i,B}}$
	mol kg^{-1}	$Pa^{-V_{i,A}}$	dimensionless	mol kg^{-1}	$Pa^{-V_{i,B}}$	dimensionless
273K	0.20416	0.00012	1.18427	4.91282	2.1244×10^{-8}	1.66553
298K	0.41214	0.0001	1	4.28732	4.28732×10^{-9}	1.68757

Table S4 Parameters for Dual-site Langmuir-Freundlich model $q_i = q_{i,A,sat}\frac{b_{i,A}p_i^{v_{i,A}}}{1+b_{i,A}p_i^{v_{i,A}}} + q_{i,B,sat}\frac{b_{i,B}p_i^{v_{i,B}}}{1+b_{i,B}p_i^{v_{i,B}}}$ adsorption of CO_2 in CeBTC at 273K and 298 K.

	Site A			Site B		
	$q_{i,A,sat}$	$b_{i,A}$	$V_{i,A}$	$q_{i,B,sat}$	$b_{i,B}$	$V_{i,B}$
	mol kg^{-1}	$Pa^{-V_{i,A}}$	dimensionless	mol kg^{-1}	$Pa^{-V_{i,B}}$	dimensionless
273K	0.42816	0.00014	1	4.23013	4.9816×10^{-9}	1.79662
298K	0.37961	0.00006	1	4.30705	9.6616×10^{-9}	1.59219

Table S5 Parameters for Dual-site Langmuir-Freundlich model $q_i = q_{i,A,sat}\frac{b_{i,A}p_i^{v_{i,A}}}{1+b_{i,A}p_i^{v_{i,A}}} + q_{i,B,sat}\frac{b_{i,B}p_i^{v_{i,B}}}{1+b_{i,B}p_i^{v_{i,B}}}$ adsorption of CO_2 in PrBTC at 273K and 298 K.

	Site A			Site B		
	$q_{i,A,sat}$ mol kg^{-1}	$b_{i,A}$ $Pa^{-V_{i,A}}$	$V_{i,A}$ dimensionless	$q_{i,B,sat}$ mol kg^{-1}	$b_{i,B}$ $Pa^{-V_{i,B}}$	$V_{i,B}$ dimensionless
273K	0. 41361	0.00028	1	5.28662	6.1637×10^{-9}	1.77175
298K	0.04791	1.64385	1.33973	26.9962	1.2468×10^{-6}	1

Table S6 Parameters for Dual-site Langmuir-Freundlich model $q_i = q_{i,A,sat}\frac{b_{i,A}p_i^{v_{i,A}}}{1+b_{i,A}p_i^{v_{i,A}}} + q_{i,B,sat}\frac{b_{i,B}p_i^{v_{i,B}}}{1+b_{i,B}p_i^{v_{i,B}}}$ adsorption of CO_2 in NdBTC at 273K and 298 K.

	Site A			Site B		
	$q_{\mathrm{i,A},sat}$	$b_{\mathrm{i,A}}$	$V_{\mathrm{i,A}}$	$q_{\mathrm{i,B},sat}$	$b_{\mathrm{i,B}}$	$V_{\mathrm{i,B}}$
	mol kg^{-1}	$Pa^{-V_{i,A}}$	dimensionless	mol kg^{-1}	$Pa^{-V_{i,B}}$	dimensionless
273K	0. 43635	0.00017	1	4.69971	4.2607×10^{-9}	1.80036
298K	7.8	4.6074×10^{-7}	1.13581	4.85108	1.2468×10^{-6}	1

Table S7 Parameters for Dual-site Langmuir-Freundlich model $q_i = q_{i,A,sat}\frac{b_{i,A}p_i^{v_{i,A}}}{1+b_{i,A}p_i^{v_{i,A}}} + q_{i,B,sat}\frac{b_{i,B}p_i^{v_{i,B}}}{1+b_{i,B}p_i^{v_{i,B}}}$ adsorption of CO_2 in SmBTC at 273K and 298 K.

	Site A			Site B		
	$q_{\mathrm{i,A},sat}$	$b_{\mathrm{i,A}}$	$V_{\mathrm{i,A}}$	$q_{\mathrm{i,B},sat}$	$b_{\mathrm{i,B}}$	$V_{\mathrm{i,B}}$
	mol kg^{-1}	$Pa^{-V_{i,A}}$	dimensionless	mol kg^{-1}	$Pa^{-V_{i,B}}$	dimensionless
273K	4.39893	7.3337×10^{-9}	1.75623	0.30948	0.00031	1
298K	2.5971	1.3041×10^{-6}	1	17.20541	1.304×10^{-6}	1

Table S8 Parameters for Dual-site Langmuir-Freundlich model $q_i = q_{i,A,sat}\frac{b_{i,A}p_i^{v_{i,A}}}{1+b_{i,A}p_i^{v_{i,A}}} + q_{i,B,sat}\frac{b_{i,B}p_i^{v_{i,B}}}{1+b_{i,B}p_i^{v_{i,B}}}$ adsorption of CO_2 in EuBTC at 273K and 298 K.

	Site A			Site B		
	$q_{i,A,sat}$ mol kg^{-1}	$b_{i,A}$ $Pa^{-V_{i,A}}$	$V_{i,A}$ dimensionless	$q_{i,B,sat}$ mol kg^{-1}	$b_{i,B}$ $Pa^{-V_{i,B}}$	$V_{i,B}$ dimensionless
273K	4.15186	3.1961×10^{-9}	1.83005	0.55916	0.00012	0.96928
298K	21.98083	6.9908×10^{-7}	1	11.92061	6.9912×10^{-7}	1

Table S9 Parameters for Dual-site Langmuir-Freundlich model $q_i = q_{i,A,sat}\frac{b_{i,A}p_i^{v_{i,A}}}{1 + b_{i,A}p_i^{v_{i,A}}} + q_{i,B,sat}\frac{b_{i,B}p_i^{v_{i,B}}}{1 + b_{i,B}p_i^{v_{i,B}}}$ adsorption of CO_2 in GdBTC at 273K and 298 K.

	Site A			Site B		
	$q_{\mathrm{i,A},sat}$	$b_{\mathrm{i,A}}$	$V_{\mathrm{i,A}}$	$q_{\mathrm{i,B},sat}$	$b_{\mathrm{i,B}}$	$V_{\mathrm{i,B}}$
	mol kg^{-1}	$Pa^{-V_{i,A}}$	dimensionless	mol kg^{-1}	$Pa^{-V_{i,B}}$	dimensionless
273K	0.09585	0.00016	1.23027	5.18978	6.847×10^{-8}	1.52651
298K	2.20943	0.00001	1	2.76337	1.6824×10^{-10}	1.94055

Table S10 Parameters for Dual-site Langmuir-Freundlich model $q_i = q_{i,A,sat}\frac{b_{i,A}p_i^{v_{i,A}}}{1+b_{i,A}p_i^{v_{i,A}}} + q_{i,B,sat}\frac{b_{i,B}p_i^{v_{i,B}}}{1+b_{i,B}p_i^{v_{i,B}}}$ adsorption of CO_2 in TbBTC at 273K and 298 K.

	Site A			Site B		
	$q_{\mathrm{i,A},sat}$ mol kg^{-1}	$b_{\mathrm{i,A}}$ $Pa^{-V_{i,A}}$	$V_{\mathrm{i,A}}$ dimensionless	$q_{\mathrm{i,B},sat}$ mol kg^{-1}	$b_{\mathrm{i,B}}$ $Pa^{-V_{i,B}}$	$V_{\mathrm{i,B}}$ dimensionless
273K	0.19639	0.00012	1.11258	5.01274	2.2408×10^{-8}	1.63889
298K	0.76313	0.00003	1	3.74467	1.7191×10^{-9}	1.73873

Table S11 Parameters for Dual-site Langmuir-Freundlich model $q_i = q_{i,A,sat}\frac{b_{i,A}p_i^{v_{i,A}}}{1+b_{i,A}p_i^{v_{i,A}}} + q_{i,B,sat}\frac{b_{i,B}p_i^{v_{i,B}}}{1+b_{i,B}p_i^{v_{i,B}}}$ adsorption of CO_2 in DyBTC at 273K and 298 K.

	Site A			Site B		
	$q_{\mathrm{i,A},sat}$ mol kg^{-1}	$b_{\mathrm{i,A}}$ $Pa^{-V_{i,A}}$	$V_{\mathrm{i,A}}$ dimensionless	$q_{\mathrm{i,B},sat}$ mol kg^{-1}	$b_{\mathrm{i,B}}$ $Pa^{-V_{i,B}}$	$V_{\mathrm{i,B}}$ dimensionless
273K	0.41969	0.00006	1.08692	4.47422	4.994×10^{-9}	1.78008
298K	0.12673	0.00012	1.02862	5.80445	1.0306×10^{-7}	1.34839

Table S12 Parameters for Dual-site Langmuir-Freundlich model $q_i = q_{i,A,sat}\frac{b_{i,A}p_i^{v_{i,A}}}{1 + b_{i,A}p_i^{v_{i,A}}} + q_{i,B,sat}\frac{b_{i,B}p_i^{v_{i,B}}}{1 + b_{i,B}p_i^{v_{i,B}}}$ adsorption of CO_2 in HoBTC at 273K and 298 K.

	Site A			Site B		
	$q_{\mathrm{i,A,}sat}$ mol kg^{-1}	$b_{\mathrm{i,A}}$ $Pa^{-V_{i,A}}$	$V_{\mathrm{i,A}}$ dimensionless	$q_{\mathrm{i,B,}sat}$ mol kg^{-1}	$b_{\mathrm{i,B}}$ $Pa^{-V_{i,B}}$	$V_{\mathrm{i,B}}$ dimensionless
273K	0.18672	0.00027	1	4.29593	3.2771×10^{-8}	1.6079
298K	4.98662	1.3954×10^{-6}	1	11.43787	1.3953×10^{-6}	1

Table S13 Parameters for Dual-site Langmuir-Freundlich model $q_i = q_{i,A,sat}\frac{b_{i,A}p_i^{v_{i,A}}}{1+b_{i,A}p_i^{v_{i,A}}} + q_{i,B,sat}\frac{b_{i,B}p_i^{v_{i,B}}}{1+b_{i,B}p_i^{v_{i,B}}}$ adsorption of CO_2 in ErBTC at 273K and 298 K.

	Site A			Site B		
	$q_{i,A,sat}$ mol kg^{-1}	$b_{i,A}$ $Pa^{-V_{i,A}}$	$V_{i,A}$ dimensionless	$q_{i,B,sat}$ mol kg^{-1}	$b_{i,B}$ $Pa^{-V_{i,B}}$	$V_{i,B}$ dimensionless
273K	0.55762	0.00007	1	4.48526	6.3441×10^{-9}	1.74989
298K	0.71984	0.00003	1	4.12892	5.4955×10^{-9}	1.62636

Table S14 Parameters for Dual-site Langmuir-Freundlich model $q_i = q_{i,A,sat}\frac{b_{i,A}p_i^{v_{i,A}}}{1+b_{i,A}p_i^{v_{i,A}}} + q_{i,B,sat}\frac{b_{i,B}p_i^{v_{i,B}}}{1+b_{i,B}p_i^{v_{i,B}}}$ adsorption of CO_2 in TmBTC at 273K and 298 K.

	Site A			Site B		
	$q_{\mathrm{i,A},sat}$	$b_{\mathrm{i,A}}$	$V_{\mathrm{i,A}}$	$q_{\mathrm{i,B},sat}$	$b_{\mathrm{i,B}}$	$V_{\mathrm{i,B}}$
	mol kg^{-1}	$Pa^{-V_{i,A}}$	dimensionless	mol kg^{-1}	$Pa^{-V_{i,B}}$	dimensionless
273K	0.40063	0.00008	1.06387	4.41645	6.9935×10^{-9}	1.7453
298K	0.91952	0.00002	1	3.53568	1.9376×10^{-9}	1.72018

Table S15 Parameters for Dual-site Langmuir-Freundlich model $q_i = q_{i,A,sat}\frac{b_{i,A}p_i^{v_{i,A}}}{1 + b_{i,A}p_i^{v_{i,A}}} + q_{i,B,sat}\frac{b_{i,B}p_i^{v_{i,B}}}{1 + b_{i,B}p_i^{v_{i,B}}}$ adsorption of CO_2 in YbBTC at 273K and 298 K.

	Site A			Site B		
	$q_{\mathrm{i,A},sat}$	$b_{\mathrm{i,A}}$	$V_{\mathrm{i,A}}$	$q_{\mathrm{i,B},sat}$	$b_{\mathrm{i,B}}$	$V_{\mathrm{i,B}}$
	mol kg^{-1}	$Pa^{-V_{i,A}}$	dimensionless	mol kg^{-1}	$Pa^{-V_{i,B}}$	dimensionless
273K	0.84421	0.00004	1	4.74373	7.9176×10^{-9}	1.72125
298K	2.60282	8.9827×10^{-6}	1	2.64936	5.3414×10^{-10}	1.83798

Table S16 Parameters for Dual-site Langmuir-Freundlich model $q_i = q_{i,A,sat}\frac{b_{i,A}p_i^{v_{i,A}}}{1+b_{i,A}p_i^{v_{i,A}}} + q_{i,B,sat}\frac{b_{i,B}p_i^{v_{i,B}}}{1+b_{i,B}p_i^{v_{i,B}}}$ adsorption of CO_2 in YBTC at 273K and 298 K.

	Site A			Site B		
	$q_{\mathrm{i,A},sat}$	$b_{\mathrm{i,A}}$	$V_{\mathrm{i,A}}$	$q_{\mathrm{i,B},sat}$	$b_{\mathrm{i,B}}$	$V_{\mathrm{i,B}}$
	mol kg^{-1}	$Pa^{-V_{i,A}}$	dimensionless	mol kg^{-1}	$Pa^{-V_{i,B}}$	dimensionless
273K	0.90016	0.00007	1	5.73706	2.7437×10^{-9}	1.81883
298K	0.17403	0.00024	1	7.47165	1.1586×10^{-7}	1.34242

Table S17 Langmuir parameters of CH_4 and N_2 for LOFs.

		CH_4		N_2	
	Temperature	q_{sat}	k_i	q_{sat}	k_i
LaBTC	273K	6.20549	1.886×10^{-6}	2.89855	9.586×10^{-7}
	298K	2.79824	2.5561×10^{-6}	1.82361	1.0532×10^{-6}
CeBTC	273K	5.61474	2.0342×10^{-6}	2.89914	9.7922×10^{-7}
	298K	3.99522	1.594×10^{-6}	1.8401	1.1468×10^{-6}
PrBTC	273K	7.20504	1.9515×10^{-6}	2.54257	1.3859×10^{-6}
	298K	7.10791	1.1439×10^{-6}	5.67019	4.2434×10^{-7}
NdBTC	273K	6.20549	1.886×10^{-6}	2.89855	9.586×10^{-7}
	298K	2.79824	2.5561×10^{-6}	1.82361	1.0532×10^{-6}
SmBTC	273K	5.29878	2.3959×10^{-6}	4.61146	6.8443×10^{-7}
	298K	4.7191	1.4301×10^{-6}	3.24326	5.8717×10^{-7}
EuBTC	273K	5.46921	2.417×10^{-6}	3.86655	8.3231×10^{-7}
	298K	5.06842	1.3435×10^{-6}	3.13592	6.1172×10^{-7}
GdBTC	273K	5.90849	2.2805×10^{-6}	10.23528	3.1699×10^{-7}
	298K	5.4561	1.4002×10^{-6}	1.49962	9.9816×10^{-7}
TbBTC	273K	5.63768	2.5004×10^{-6}	3.74192	8.9655×10^{-7}
	298K	4.92437	1.4818×10^{-6}	3.32569	6.2206×10^{-7}
DyBTC	273K	5.26047	2.6474×10^{-6}	4.61591	7.5032×10^{-7}
	298K	3.98193	1.824×10^{-6}	4.17247	4.9665×10^{-6}
HoBTC	273K	4.97104	2.4934×10^{-6}	4.83234	6.2271×10^{-7}
	298K	4.07771	1.5147×10^{-6}	2.39017	6.9737×10^{-7}
ErBTC	273K	5.78784	2.42×10^{-6}	11.21196	2.8818×10^{-7}
	298K	5.17664	1.5013×10^{-6}	11.21157	2.8919×10^{-7}
TmBTC	273K	5.16136	2.7871×10^{-6}	3.29764	1.0369×10^{-6}
	298K	4.61577	1.6555×10^{-6}	2.57521	8.0296×10^{-7}
YbBTC	273K	7.52263	1.9667×10^{-6}	5.36348	6.5993×10^{-7}
	298K	5.70166	1.5267×10^{-6}	12.69796	1.7862×10^{-7}
YBTC	273K	6.5055	2.7462×10^{-6}	4.95758	8.8898×10^{-7}
	298K	5.276	1.8277×10^{-6}	6.89978	2.7539×10^{-7}

Table S18 The sample mass of the activated LnBTC for breakthrough experiments.

LnBTC	**LaBTC**	**CeBTC**	**PrBTC**	**NdBTC**	**SmBTC**	**EuBTC**	**GdBTC**	**TbBTC**	**DyBTC**	**HoBTC**	**ErBTC**	**TmBTC**	**YbBTC**	**YBTC**
mass(g)	1.0611	0.9131	1.1326	1.4996	0.9004	0.5428	0.689	1.0512	0.8324	0.647	0.8615	0.5302	0.6259	0.9417